

## BIOPHYSICS

# Efficacy and specificity of inhibitors of BCL-2 family protein interactions assessed by affinity measurements in live cells

Elizabeth J. Osterlund<sup>1,2</sup>, Nehad Hirmiz<sup>1,3</sup>, James M. Pemberton<sup>1,4</sup>, Adrien Nougarède<sup>1</sup>, Qian Liu<sup>1</sup>, Brian Leber<sup>5</sup>, Qiyan Fang<sup>3,6</sup>, David W. Andrews<sup>1,2,4\*</sup>

Cytoplasmic and membrane-bound BCL-2 family proteins regulate apoptosis, a form of programmed cell death, via dozens of binary protein interactions confounding measurement of the effects of inhibitors in live cells. In cancer, apoptosis is frequently dysregulated, and cell survival depends on antiapoptotic proteins binding to and inhibiting proapoptotic BH3 proteins. The clinical success of BH3 mimetic inhibitors of antiapoptotic proteins has spawned major efforts by the pharmaceutical industry to develop molecules with different specificities and higher affinities. Here, quantitative fast fluorescence lifetime imaging microscopy enabled comparison of BH3 mimetic drugs in trials and preclinical development by measuring drug effects on binding affinities of interacting protein pairs in live cells. Both selectivity and efficacy were assessed for 15 inhibitors of four antiapoptotic proteins for each of six BH3 protein ligands. While many drugs target the designed interaction, most also have unexpected selectivity and poor efficacy in cells.

## INTRODUCTION

B-cell lymphoma 2 (BCL-2) family protein interactions regulate the permeabilization of mitochondria that commits a cell to undergo apoptosis. Up-regulation of the antiapoptotic BCL-2 family proteins BCL-2, BCL-XL, BCL-W, and MCL-1 enables cancer cell survival. Antiapoptotic proteins are inhibited by binding to “BH3 proteins” that are so named because they share a single common peptide sequence called a BCL-2 homology 3 (BH3) motif essential for proapoptotic function (Fig. 1A) (1–5). Some BH3 proteins both inhibit antiapoptotic proteins and trigger proapoptotic pore-forming proteins to permeabilize the mitochondria outer membrane. For these proteins, interaction with antiapoptotic proteins results in mutual sequestration both inhibiting and promoting cell survival (Fig. 1B). Small molecules that mimic the BH3 motif release proapoptotic proteins restoring apoptosis cells. However, selective inhibition of antiapoptotic BCL-2 family proteins responsible for cancer cell survival is particularly challenging since the shared features within BH3 motifs are limited to four to five residues, yet all bind to the individual BH3 binding pockets of one or more of the antiapoptotic proteins. Small differences in the BH3 regions and binding pockets, therefore, govern the affinities of the BCL-2 family interactions that regulate cell death (6, 7).

Although targeting protein-protein interactions is challenging, there have been recent successes in generating BH3 mimetic drugs that inhibit antiapoptotic proteins, including venetoclax (ABT-199), a BCL-2 inhibitor recently approved by the U.S. Food and Drug Administration (FDA) for treatment of leukemias (8, 9), and navitoclax (ABT-263), an in-trial anticancer drug that inhibits BCL-2,

BCL-XL, and BCL-W (10–12). These drugs not only are revolutionizing patient treatment but also have provided previously unidentified into the molecular mechanisms that regulate cell death. Many BH3 mimetics are now under development (Fig. 1C) (10, 13–20), the majority of which were tested using truncated purified proteins missing the membrane-binding domains and BH3 peptides because of difficulties purifying full-length membrane-binding proteins. The combinatorial nature of BCL-2 family interactions and the various modifying regulatory mechanisms including subcellular localization and posttranslational modifications have made extrapolation of measurements made with purified protein fragments to cellular outcomes unreliable. Furthermore, both effective BH3 mimetics and toxic compounds kill cells, making measurements based on biological outcomes difficult to interpret.

Both the dissection of cell signaling pathways and drug development efforts would be greatly aided if protein-protein interactions could be rapidly quantified in live cells. However, such measurements remain extremely challenging, and commonly used techniques such as proximity ligation (21), protein complementation (22), and bioluminescence resonance energy transfer (BRET) (23) report only proximity, are confounded by collisions, and do not permit reliable quantification of changes in binding affinities. Unlike these techniques, Förster resonance energy transfer (FRET) can be used to measure protein-protein interactions with high spatial resolution (see Table 1 for definitions of technical terms). In cells, fluorescence lifetime imaging microscopy (FLIM) is ideal for measuring FRET because the time a population of donor fluorophores remains in the excited state before returning to the ground state is independent of changes in fluorescence intensity that complicate other methods of measuring FRET (24). We recently compared two BH3 mimetics for inhibition of BCL-XL binding to three BH3 proteins using FLIM-FRET to obtain an arbitrary measure of “drug resistance” (25, 26). Unexpectedly, in live cells, both the efficacy and specificity of navitoclax were different than predicted from cell-free measurements (25–27), suggesting that other BH3 mimetics will have unexpected properties when assayed in live cells. As many of these

Copyright © 2022  
The Authors, some  
rights reserved;  
exclusive licensee  
American Association  
for the Advancement  
of Science. No claim to  
original U.S. Government  
Works. Distributed  
under a Creative  
Commons Attribution  
NonCommercial  
License 4.0 (CC BY-NC).

<sup>1</sup>Biological Sciences, Sunnybrook Research Institute, Toronto, Ontario M4N 3M5, Canada. <sup>2</sup>Department of Biochemistry, University of Toronto, Toronto, Ontario M5S 2J7, Canada. <sup>3</sup>School of Biomedical Engineering, McMaster University, Hamilton, Ontario L8S 4L7, Canada. <sup>4</sup>Department of Medical Biophysics, University of Toronto, Toronto, Ontario M5S 2J7, Canada. <sup>5</sup>Department of Medicine, McMaster University, Hamilton, Ontario L8N 3Z5, Canada. <sup>6</sup>Department of Engineering Physics, McMaster University, 1280 Main Street West, Hamilton, Ontario L8S 4L7, Canada.  
\*Corresponding author. Email: david.andrews@sri.utoronto.ca

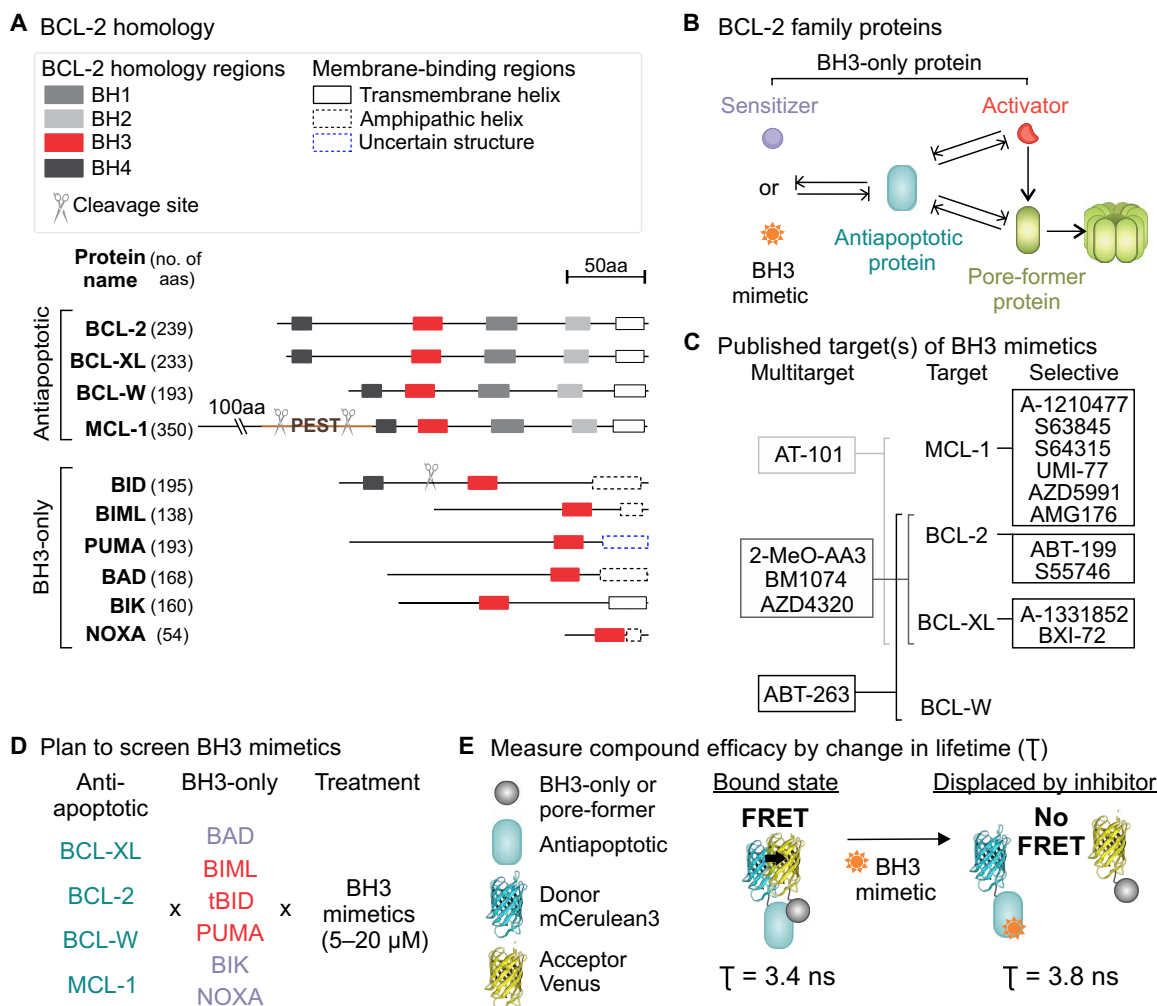


**Fig. 1. Determining efficacy and selectivity of BH3 mimetic compounds against antiapoptotic proteins in live cells.** (A) Schematic representations of the human amino acid (aa) sequence for the analyzed BCL-2 family proteins (1–5). BH regions are indicated with numbers 1 to 4, with the BH3 region indicated in red; membrane-binding region types are specified. A 50aa scale is shown; 100aa in MCL-1 were removed to fit it in the figure. Locations of cleavage sites (scissors) and the proline (P), glutamic acid (E), serine (S), threonine (T) enriched sequence (PEST) in MCL-1 are shown. (B) Schematic of BCL-2 family protein interactions. Capped arrows indicate mutual sequestration (inhibition of both proteins as a result of binding). Arrows represent activation. (C) Published specificities of BH3 mimetics tested here (10, 13–20). (D) Interactions to be probed with BH3 mimetics in our screen. Protein names are colored according to their functional group in (B). (E) Schematic of an interaction between an antiapoptotic protein fused to mCerulean3 fluorophore and a proapoptotic protein fused to Venus fluorophore being displaced by a BH3 mimetic drug. Energy transfer (FRET) from mCerulean3 to Venus (black arrow) only occurs when the two proteins bind. A BH3 mimetic drug (\*) binds the antiapoptotic protein and disrupts this complex. Lifetime ( $\tau$ ) of mCerulean3 in both bound and unbound states is shown below. See also fig. S1.

molecules are now entering clinical trials, proper trial design and patient selection would be greatly aided by a better understanding of the specificity and efficacy of BH3 mimetics in live cells. However, the number of BH3 mimetics tested has been limited since commercial FLIM-FRET systems are low throughput and do not generally permit calculation of binding affinities.

Our aim was to directly compare BH3 mimetics by measuring the disruption of several full-length BCL-2 family interactions in live cells (Fig. 1, D and E), requiring advancements to the FLIM-FRET method. The quantitative fast FLIM-FRET ( $qF^3$ ) method that we introduce here can be used to rapidly quantify the effects of drugs, mutations, and competition on protein-protein interactions in live cells. To enable  $qF^3$ , we built a multiplexed instrument with rapid data acquisition and developed specialized software to permit automated determination of the effects of drugs on protein-protein

interactions measured directly in living cells. By also incorporating standard curves for the expressed proteins, it was possible to determine apparent dissociation constant ( $K_d$ ) values in subcellular regions of live cells (28). Using  $qF^3$ , we measured for 15 promising BH3 mimetics concentration-dependent disruption of 24 unique BCL-2 family protein-protein complexes in a physiologically relevant context. For the majority of these compounds, we provide the first quantitative measurement of selectivity and efficacy in live cells. Unexpectedly, for every compound, we report differences in binding efficacy and/or selectivity in live cells from that predicted based on measurements made using purified protein fragments and peptides. This information is critically important, as drugs targeting BCL-2 family interactions are marching toward the clinic at an accelerating pace. The large dataset that we provide here also contributes to understanding the cell biology underpinning the

**Table 1. List of technical terms used here.**

Term used here	Information
Ground state	The lowest quantized electronic state for a fluorescent molecule.
Excited state	Quantized electronic state that has higher energy than the ground state.
Fluorophore	A protein that absorbs light energy at a particular wavelength ( $\lambda$ ), enters an excited state, and then emits light at a longer $\lambda$ . Return to the ground state is achieved by the emission of energy in the form of a photon. Some energy is lost to vibrations/heat, etc. Thus, the emitted light has lower energy than the excitation source.
Fluorescence lifetime or lifetime	The average time that a population of fluorophores remains in the excited state before returning to the ground state. Lifetime is a physical property of the donor that is environment sensitive but concentration independent. Lifetime is measured on the nanosecond scale.
Excitation spectra	The distribution of wavelengths of light that excite a fluorescent molecule.
Emission spectra	The distribution of wavelengths of light emitted by a fluorescent molecule.
FRET	Förster resonance energy transfer. Nonradiative energy transfer between two light-sensitive molecules.
FRET pair or acceptor:donor pair	Two fluorophores with overlapping spectra, suitable for efficient FRET: The emission spectra of the donor overlap with the excitation spectra of the acceptor.
Donor	Donor fluorophore. During FRET, the donor donates (or transfers) its excited state energy to an acceptor fluorophore, thereby returning to the ground state. FRET decreases the observed intensity and fluorescence lifetime of the donor.
mCerulean3	Donor fluorophore used here, monomeric cyan fluorescent protein. Sometimes shortened to "mCer3." Excitation $\lambda$ , 433 nm; emission $\lambda$ , 475 nm; lifetime, 3.8 ns.
Acceptor	Acceptor fluorophore. During FRET, the acceptor accepts energy from the excited donor fluorophore and, in turn, enters its excited energy state. The excited acceptor fluorophore then emits energy at a longer wavelength before returning to the ground state. FRET increases the observed intensity of the acceptor.
Venus	Acceptor fluorophore used here, monomeric yellow fluorescent protein. Excitation $\lambda$ , 515 nm; emission $\lambda$ , 527 nm; lifetime, 2.9 ns.
Venus <sub>Free</sub>	Unbound Venus
Fluorescence lifetime decay	A plot correlating the number of single photons emitted from a sample over time after a short, pulsed excitation. Used to calculate the average fluorescence lifetime of the sample.
FLIM	Fluorescence lifetime imaging microscopy.
FLIM-FRET	Using FLIM to measure FRET. Lifetime of the donor decreases with FRET.
FRET-stimulated emission	Intensity emitted from acceptor (Venus) molecules that were excited directly by energy transfer from the donor (mCerulean3) rather than the pulsed excitation source.
TCSPC	Time-correlated single-photon counting. Technique to measure fluorescence lifetime decays. A pulsed laser with a high repetition rate excites the population of fluorophores in the sample. The arrival time of single-photon events is recorded. With many repetitions, the photon distribution is built up over the total acquisition time. The spatial coordinates of arriving photons are stored to generate a map of fluorescence lifetime decay curves across the image.
Intensity at time 0 (T <sub>0</sub> )	The first part of the fluorescence lifetime decay, immediately after excitation of the fluorophore. Since FRET is a process that occurs on a nanosecond scale, there is a low probability that fluorophores that emit at T <sub>0</sub> undergo FRET. Thus, the intensity at T <sub>0</sub> is directly proportional to the total number of fluorophores in the excitation volume.
IRF	Instrument response function. Excitation pulses are not infinitely narrow (delta function). In addition, the response of electronic detectors exhibits a delay since photons must be first absorbed before generating a signal. The combination of the two effects produces a broadening effect in our single-photon detection signal. The IRF is a temporal profile of the scattered excitation light, specific to the instrument/sample used, that is, used to correct for this broadening effect.
qF <sup>3</sup>	Quantitative fast FLIM-FRET. A method established here to generate quantitative live-cell binding curves for protein-protein interactions and determine live-cell binding affinities (apparent $K_d$ ) that are used as a readout for high-content screening applications.
G factor	Factor calculated for the microscope at filter settings chosen for data acquisition. The G factor is used to estimate and subtract the intensity observed in the acceptor channel due to FRET-stimulated emission from the acceptor.

continued on next page

Term used here	Information
ROI	Region of interest. In our case, these are small subcellular areas, automatically selected via a Watershed algorithm, where the pixels are binned together.
Bleed-through	Overlapping emission wavelengths of two fluorophores can muddy the signal and interfere with making accurate intensity measurements. Bleed-through occurs when one fluorophore emits at the same wavelength and at the same time that another fluorophore is detected. Here, for example, mCerulean3 emission overlaps with that of Venus, and this signal must be subtracted before an accurate measure of Venus intensity can be made.
Cross-talk	Overlapping excitation wavelengths of two fluorophores can muddy the signal and interfere with making accurate intensity measurements. Cross-talk occurs when two or more fluorophores in a sample are excited with the same wavelength at the same time because their excitation spectra partially overlap.
Phasor analysis	Mathematical representation of data in Fourier space. The fluorescence lifetime decay curve is Fourier-transformed and displayed on the universal semicircle. This essentially represents the lifetime decay as a combination of cosine (horizontal axis $G$ ) and sine (vertical axis $S$ ) functions. The phasor approach to determining lifetime is quick, computationally inexpensive, and does not require fitting.
Collisional control	The negative control in a FLIM-FRET experiment. A nonbinding mutant or nonbinding acceptor fusion protein with similar subcellular localization as the positive control. We use "BH3-4E" mutants as our collisional controls for each BH3 protein tested.
Angular frequency ( $\omega$ )	In the Fourier space, the angular frequency gives the proportion of cosines and sine components of the fluorescent lifetime decay and is represented as the angle between the signal vector and the horizontal (cosine) axis on a phasor plot.
$\Delta\omega$	The fractional change in angular frequency occurs in the presence of FRET. FRET increases the rate of fluorescence decay (shorter fluorescence lifetime), and the proportion of cosine:sine components increases, which "pulls" the signal vector toward the sine axis. $\Delta\omega$ is directly related to the fraction of donor molecules in the bound versus unbound state.
$\Delta\beta$	The maximum difference in median $\Delta\omega$ of test well ( $^V$ BH3) compared to its collisional control ( $^V$ BH3-4E) in the absence of added drug.
sRatio	Shape ratio: The ratio of the area above divided by the area below the isotonic fit of the binned binding curve data. sRatio is independent of $\Delta\beta$ and is calculated without fitting data to a Hill slope. This value describes the shape of the curve. A completely straight line will have an sRatio = 1. Higher sRatios (>2) indicate binding curve saturation. Thus, we use the sRatio to automatically decide whether to proceed with fitting the data to determine apparent $K_d$ .
%Resistance (% $R$ ) or %Drug resistance	Established in (26) as a means of quantifying the amount of resistance of a protein-protein interaction to displacement by chemical or mutational intervention. Determined at a single point on the binding curve (in our case, between 10 and 20 $\mu$ M Venus <sub>FRET</sub> ). % $R$ is equal to 1 minus the difference between the test well ( $^V$ BH3) and the collisional control ( $^V$ BH3-4E) divided by $\Delta\beta$ . On a scale of 0 to 100%, lower %Resistance is equal to higher drug efficacy.
Hyperspectral	Many wavelengths are separately imaged and stored together. Our hyperspectral module divides the emitted signal into 64 wavelength bins.
Channel	A channel can refer to the detection of a selected range of wavelengths or a specific type of data. For example, "Blue, Green, Red, FarRed" channels were collected on the Opera Phenix microscope. We also use "channel" when referring to the INO-FHS data, to indicate the type of data collected. In this case, the "TCSPC channel" refers to the TCSPC data, collected for the donor (mCerulean3) and used to generate the FLIM image. The "hyperspectral channel" refers to the wavelengths detected by the hyperspectral module, including the range of acceptor (Venus) intensity.
SPAD	Single-photon avalanche photodiode. A type of detector that is used to collect TCSPC channel data on the INO-FHS platform.
PMT	Photomultiplier tube. This type of detector is used to collect hyperspectral channel data on the INO-FHS platform.
INO-FHS	INO-FLIM hyperspectral. A microscope built for our laboratory to rapidly collect FLIM data and simultaneously collect hyperspectral image data.
Interleaved excitation	With a pulsed laser source, interleaved excitation refers to rapidly switching back and forth between excitation of the donor and excitation of the acceptor. Essentially, the two channels are collected simultaneously while minimizing cross-talk.

molecular mechanisms that regulate apoptosis and reveals previously unidentified insights into this promising class of anticancer drugs.

**RESULTS**

**High-content screening by automated qF<sup>3</sup>**

Here, we report measurements for BCL-2 family proteins and the drugs that inhibit their interactions using proteins expressed as fusions to either mCerulean3 (as donor) or Venus (as acceptor) fluorescence proteins (Fig. 1E). The superscript “C” or “V” preceding a protein name indicates N-terminal fusion of mCerulean3 or Venus, respectively. Binding measurements reported are based on changes in the donor (mCerulean3) fluorescence lifetime and the measured concentrations of both donor and acceptor. Given that the antiapoptotic protein is the target of both BH3 protein and BH3 mimetic inhibitor drugs, we express the antiapoptotic protein stably in the cell line of interest, then transiently transfect the Venus (acceptor)-fused BH3 protein, and then treat with drug or solvent [dimethyl sulfoxide (DMSO)] control. Transient expression of the

acceptor ensures sufficient variation in concentration to enable plotting a binding curve. Drugs are assessed as changes in the binding curve summarized as apparent binding constants in heatmaps. To avoid complications due to dead or dying cells in our analyses, we expressed the proteins in baby mouse kidney (BMK) cells that are resistant to apoptosis because of the double gene knockout of the executioner pore-forming proteins BCL-2-associated X protein (BAX) and BCL-2 homologous antagonist killer protein (BAK) (BMK-DKO). Donor antiapoptotic proteins <sup>C</sup>BCL-XL, <sup>C</sup>BCL-2, <sup>C</sup>BCL-W, or <sup>C</sup>MCL-1 were stably expressed in BMK-DKO cells and confirmed to be functional (fig. S1, A and B). We examined the interaction between each antiapoptotic protein with the following BH3 proteins: BCL-2-associated death promoter (BAD), BCL-2-like protein 11 isoform L (BIML), truncated BH3 interacting-domain death agonist (tBID), p53 upregulated modulator of apoptosis (PUMA), BCL-2 interacting killer (BIK), and Phorbol-12-myristate-13-acetate-induced protein 1. (NOXA). The acceptor proteins; Venus-fused BH3 proteins <sup>V</sup>BAD, <sup>V</sup>BIML, <sup>V</sup>tBID, <sup>V</sup>PUMA, <sup>V</sup>BIK, and <sup>V</sup>NOXA; and their nonbinding negative control counterparts harboring a 4E mutation in the BH3 sequence that disrupts

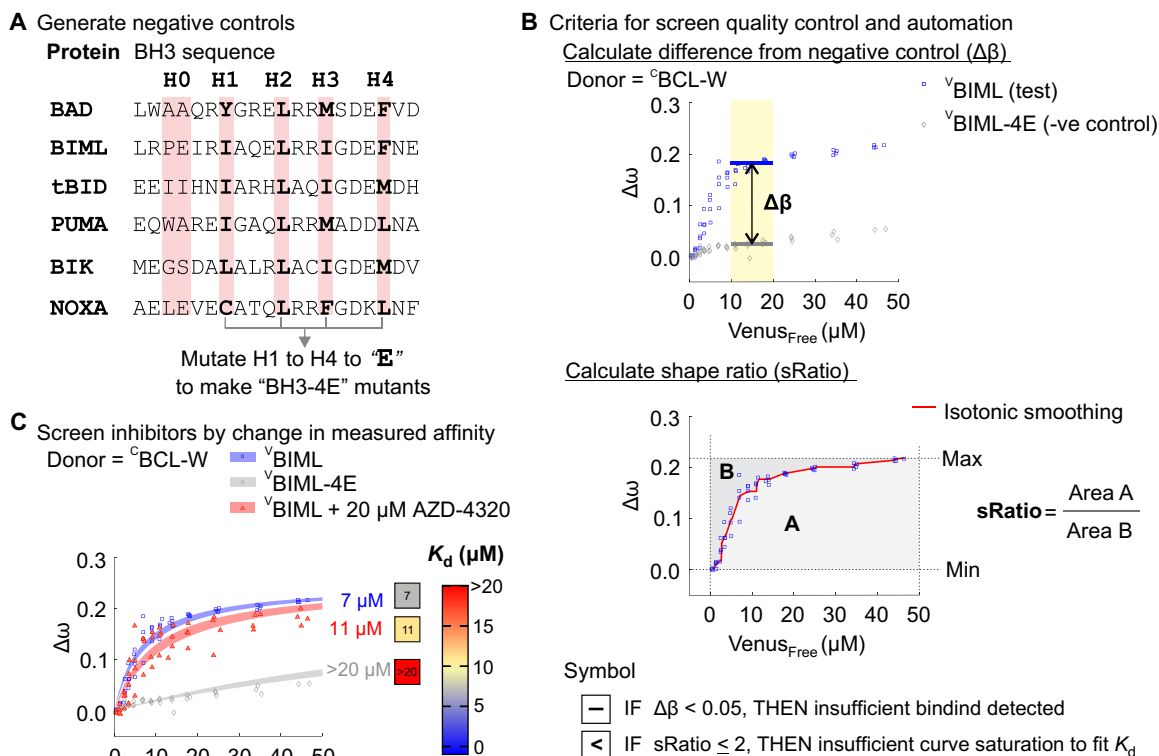


**Fig. 2. Criteria for screening BH3 mimetics by qF<sup>3</sup>.** (A) To create appropriate negative controls for qF<sup>3</sup> screening, we mutated the BH3 region to eliminate binding. The amino acid sequence of the BH3 region for each BH3 protein is shown, with the four key hydrophobic residues (pink) changed to E (glutamic acid) in the “BH3-4E” negative controls. (B) Binding curves are analyzed automatically to determine whether sufficient binding has been detected. We set two criteria for screening by qF<sup>3</sup>, illustrated here. Example curves (combined from three biological replicates) for BMK-DKO-<sup>C</sup>BCL-W cells transfected with constructs expressing test “<sup>V</sup>BIML” or negative control “<sup>V</sup>BIML-4E.” The difference in  $\Delta\omega$  for the positive and negative controls ( $\Delta\beta$ ) must be greater than 0.05, and sRatio must be greater than 2 for determination of an apparent  $K_d$ . (C) If criteria in (B) are met for screening, binding curves are fit to a Hill slope equation to determine  $K_d$ . The line thickness indicates the 95% confidence interval for the best fit. The parameters for fitting the negative and drug-treated curves are fixed on the basis of the test (positive) control. Example curves for BMK-DKO-<sup>C</sup>BCL-W cells transfected with <sup>V</sup>BIML and treated with BH3 mimetic, AZD4320. This compound has little effect on the interaction and little effect on the resulting  $K_d$ . The  $K_d$  measured is displayed in heatmap format to the right, where shades from gray to dark blue (scale on the right) indicate progressively lower  $K_d$  values. These curves represent authentic binding in cells, while red indicates an apparent  $K_d$  greater than 20  $\mu$ M and represents “lack of binding” or collisions (gray straight line). See also figs. S2 to S5.



binding to antiapoptotic proteins (Fig. 2A) displayed the expected functions in cells (fig. S1C). For the BH3 mimetics, the useful concentration range was determined by titrating the mimetics up to 20  $\mu\text{M}$ , observing off-target toxicity for only UMI-77 (fig. S1D). Concentrations of 20, 10, and 5  $\mu\text{M}$  were tested for all compounds, as these concentrations are similar to both those used previously (25–27, 29) and the in-human concentrations achieved safely for venetoclax and navitoclax (11, 12, 30–33). For selected compounds, the lowest effective concentration was determined by titration down to 0.08  $\mu\text{M}$ . FLIM-FRET measurements were made using a custom-built, high-speed, automated, and multiplexed FLIM microscope (fig. S2 and see Supplementary Text for description).

We developed the  $qF^3$  method to enable measuring in live cells both apparent affinities of protein-protein interactions and the effects of drugs on these interactions (see Materials and Methods and figs. S3 and S4 for technical details). Recognizing the strengths and weaknesses of this technique is critical for interpreting the results.  $qF^3$  is quantitative. The  $x$  axis of all of the binding curves is protein concentration, thereby standardizing the curves and allowing calculation of apparent affinities. Local concentrations of  $^C$ antiapoptotic and  $^V$ BH3 proteins were measured by direct comparison of intensity to standard curves of purified mCerulean3 and Venus proteins (fig. S3, A to D), as previously described (28), except without extrapolation. Phasor lifetime analysis (34) was used to calculate the fractional change in angular frequency ( $\Delta\omega$ ), a value directly related to the fraction of donor molecules in the bound versus unbound state enabling determination of the concentration of unbound Venus ( $Venus_{\text{Free}}$ ; see Materials and Methods) assuming 1:1 binding. As lifetime is used to define the bound and unbound state, compounds that affect the donor lifetime directly (venetoclax; see below) cannot be analyzed by  $qF^3$ . The  $qF^3$  binding curves contain data in three dimensions (fig. S4B; see example binding curve). However, changes in mCerulean3 expression had a measurable effect on apparent  $K_d$  (fig. S3, H and I), indicating that although the protein levels are similar to those in cells, the donor concentration exceeded the absolute  $K_d$  [see (35) for absolute versus apparent  $K_d$ ]. For direct quantitative comparison of the different BH3 mimetics, we condense the binding curve data to two dimensions by assaying cells with  $^C$ antiapoptotic protein expression between 1 and 3  $\mu\text{M}$ , consistent with the levels measured in cancer cells (36). As a result, the apparent affinities of the complexes are similar ( $\sim 5 \mu\text{M}$ ) unless the absolute affinity is higher than  $\sim 5 \mu\text{M}$ . This ensures that all of the drugs are tested against a similar starting concentration of complexes.

Increases in  $\Delta\omega$  indicate increased binding (FRET), which only occurs when the donor and acceptor fluorophore come within 10 nm of each other. While this generally indicates binding, two nonbinding proteins that collide can also undergo FRET; however, collisions result in a linear increase in  $\Delta\omega$  depending on the concentration of unbound (Free) Venus fusion protein expressed in cells [see Fig. 2 (B and C) for example of binding in blue versus nonbinding in gray]. Hence, it is best practice to include a negative control with the same subcellular localization as each protein of interest (our BH3-4E mutants). True binding may then be confidently identified by comparing the  $qF^3$ -derived binding curve to the negative control. Thus, false positives are extremely rare. However, the reverse is not always true: Lack of FRET does not definitively indicate that two proteins do not bind, as it can be the case that the donor and acceptor fluorophores are too far apart or that their geometry is

unfavorable. Given this limitation,  $qF^3$  is best suited for screening reduction/elimination of binding compared to a starting binding curve, i.e., the effects of drugs, mutations, and competition on protein-protein interactions in live cells.

In  $qF^3$  screening, not all data can be productively fit to a Hill equation. To automatically eliminate these samples in our analysis pipeline,  $qF^3$  includes criteria for determining the most appropriate analysis method (Fig. 2B and see fig. S4 for details). First, the maximum difference in median  $\Delta\omega$  was calculated for the BH3 protein being tested ( $^V$ BH3) and its collisional control ( $^V$ BH3-4E) in the absence of added drug ( $\Delta\beta$ ). A  $\Delta\beta$  of less than 0.05 indicates insufficient dynamic range to measure a decrease upon adding BH3 mimetic (see examples in fig. S5A). Second, we took advantage of the fact that collisions increase linearly with local concentration and calculated “shape ratio” (sRatio), a value independent of  $\Delta\beta$ , calculated without fitting, that can differentiate collisional data from binding curves (Fig. 2B). On the basis of simulated and experimental data, we set a minimum sRatio of 2 [fig. S5 (B and C) and see Materials and Methods] to proceed with fitting data to a Hill slope equation to determine  $K_d$  (Fig. 2C). If sufficient binding was detected ( $\Delta\beta > 0.05$ ) but sRatio  $< 2$ , then the binding curve did not saturate within the range sampled. We recover some information from such data by using a measure of “%drug resistance,” as described previously (26). Unlike a binding constant, %drug resistance only measures displacement at a single point in the curve. To compare large numbers of apparent binding constants in a single figure, the data are presented as heatmaps. Visually, binding is indicated by the blue color, and nonbinding is indicated by red. Thus, in heatmaps, a drug that inhibits binding is indicated by a change in color from blue to red. The corresponding numerical values are indicated within each square. For the antiapoptotic proteins  $^C$ BCL-XL,  $^C$ BCL-2,  $^C$ BCL-W, and  $^C$ MCL-1, we provide the measurements for  $\Delta\beta$  and sRatio for every  $^V$ BH3 and  $^V$ BH3-4E negative control to demonstrate why certain protein-protein interactions met or did not meet the criteria for certain  $qF^3$  analyses (Fig. 2B).

### Efficacy and selectivity of inhibitors of $^V$ BH3 binding to $^C$ BCL-2

The interactions of many BCL-2 family members have been studied using truncated proteins and BH3 peptides because of the challenges of BCL-2 family protein purification (37, 38). Of the antiapoptotic proteins, only BCL-XL is well behaved as a full-length protein in solution, and the family’s founding member, BCL-2, a constitutively membrane-bound protein (39–41), was only recently purified in full length by solubilization in detergent micelles (38). In addition, recombinant proteins expressed in prokaryotic cells may have differences in folding and posttranslational modifications that affect function. For example, detergents affect the function of many BCL-2 family members (42, 43). In contrast, screening by  $qF^3$  enables the measurement of interactions for full-length proteins and mutants in live cells. As expected, compared to the wild-type  $^V$ BH3 proteins, the binding of the BH3-4E mutants to  $^C$ BCL-2 was markedly reduced (Fig. 3A). For  $^C$ BCL-2, sufficient binding ( $\Delta\beta > 0.05$ ) (Fig. 3A) and sRatio  $\geq 2$  (Fig. 3B) were observed for all of the  $^V$ BH3 proteins, including  $^V$ NOXA [indicating binding to BCL-2, as controversially reported (44)], demonstrating the value of unbiased high-content screening [see fig. S5 (D and E) for binding curve]. The change in apparent binding constants ( $K_d$ ) provides a quantitative comparison of the efficacy of BH3 mimetics to inhibit



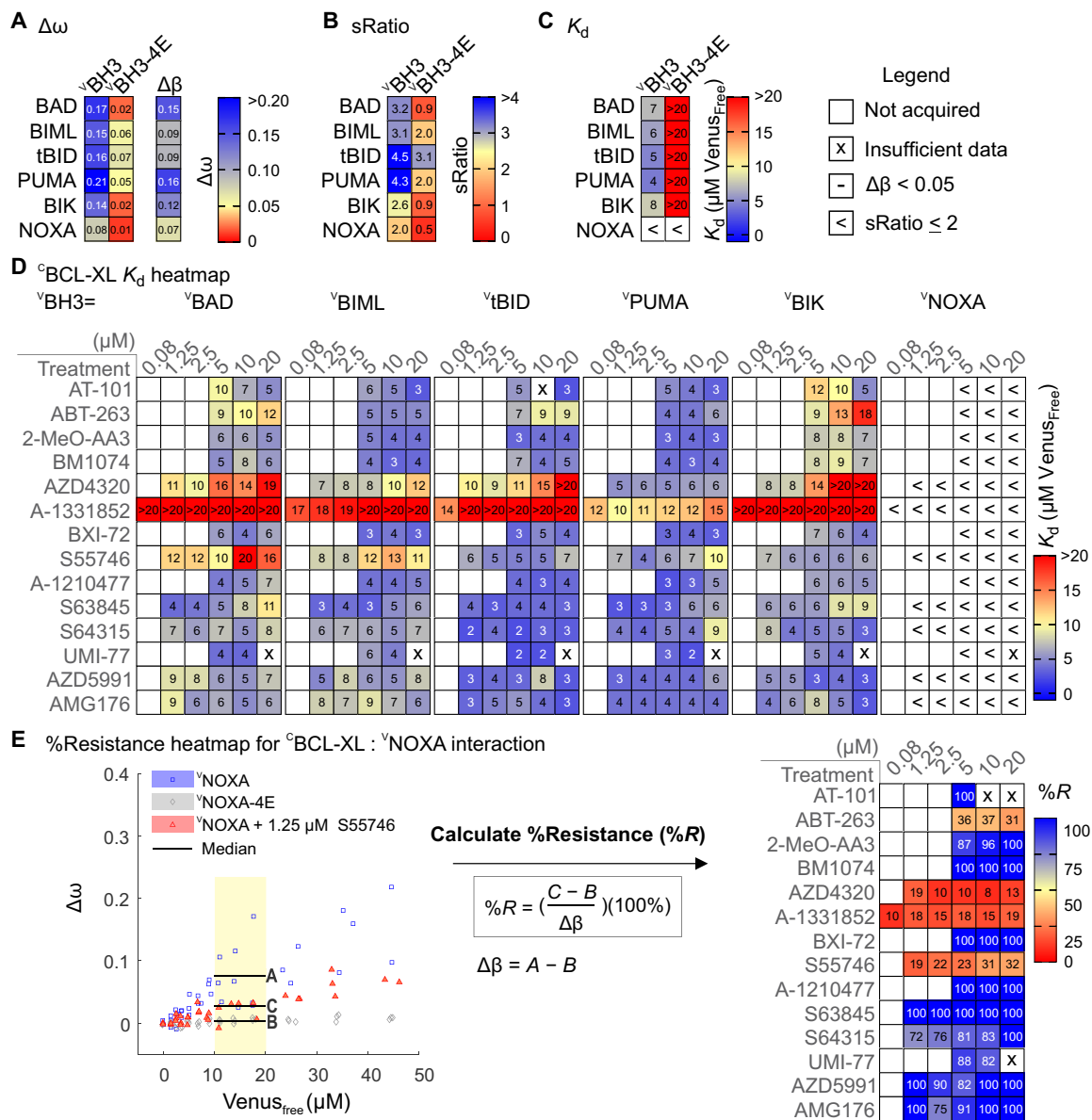


**Fig. 4. BH3 mimetic inhibition of  $\nu^{BH3}$  protein binding to  ${}^C\text{BCL-XL}$  measured by  $qF^3$ .** (A to C) Binding of  $\nu^{BH3}$  proteins to  ${}^C\text{BCL-XL}$  measured by  $qF^3$  as in Fig. 3. (A) Values for  $\Delta\omega$  and  $\Delta\beta$  for  ${}^C\text{BCL-XL}$  binding to the individual  $\nu^{BH3}$  and  $\nu^{BH3-4E}$  control proteins. (B) The sRatio for the binding of  $\nu^{BH3}$  proteins to  ${}^C\text{BCL-XL}$ . The sRatio for  $\nu^{NOXA}$  was not  $>2$ , and apparent  $K_d$ 's were not calculated (indicated " $<$ " in the heatmaps). (C) Automatically calculated apparent  $K_d$ 's for the binding interactions in micromolar. Values greater than 20 are for binding data that did not saturate (sRatio  $< 2$ ). (D) Heatmap of automatically calculated apparent  $K_d$  values for  $\nu^{BH3}$  proteins (listed on top) treated with BH3 mimetics (left) at concentrations indicated above each column. (E) Calculation of %resistance to displacement for  $\nu^{NOXA}$  binding to  ${}^C\text{BCL-XL}$  (%R). To the left are example binding curve data for  $\nu^{NOXA}$  (blue),  $\nu^{NOXA-4E}$  (gray), and  $\nu^{NOXA} + \text{drug}$  (red). The calculations for %R and of the value corresponding to  $\Delta\beta$  are shown. Similar to the analysis for calculating  $K_d$ , for a calculated %R to be meaningful,  $\Delta\beta$  should be  $>5\%$ . To the right is the %R heatmap. The more resistant the complex is to displacement (blue), the less effective the drug.

unlike other BCL-XL inhibitors, did not affect  $\nu^{tBID}$  or  $\nu^{BIK}$  binding. Sufficient binding between  $\nu^{NOXA}$  and  ${}^C\text{BCL-XL}$  was detected to verify binding; however, a low sRatio indicated insufficient saturation to accurately estimate a  $K_d$ . On the basis of measured %drug resistance,  $\nu^{NOXA}$  binding to  ${}^C\text{BCL-XL}$  was inhibited by all the effective BCL-XL inhibitors (Fig. 4E). Other BH3 mimetics previously reported to inhibit BCL-XL [bisbenzimidazole H33258 (BXI-72) (16)], BCL-2 and BCL-XL [e.g., BM1074 (45) and 2-MeO-AA3 (13)], or MCL-1 did not affect the binding of  ${}^C\text{BCL-XL}$  to  $\nu^{BH3}$  proteins.

### Efficacy and selectivity of inhibitors of $\nu^{BH3}$ binding to ${}^C\text{BCL-W}$

Direct binding of BH3 proteins to BCL-W has not been previously quantified in cells. Automated  $qF^3$  revealed that  ${}^C\text{BCL-W}$  binds preferentially to  $\nu^{BIML}$ ,  $\nu^{tBID}$ , and  $\nu^{PUMA}$  compared to  $\nu^{BAD}$  and  $\nu^{BIK}$  with no detectable binding to  $\nu^{NOXA}$  [Fig. 5 (A to C) and see fig. S5D for curve data]. As seen for  ${}^C\text{BCL-2}$  and  ${}^C\text{BCL-XL}$ , binding of  ${}^C\text{BCL-W}$  to  $\nu^{PUMA}$  was refractory to all inhibitors (Fig. 5D). Unexpectedly, BCL-2/BCL-XL/BCL-W inhibitor ABT-263 (10) effectively inhibited binding of  ${}^C\text{BCL-W}$  to only  $\nu^{BAD}$ ,



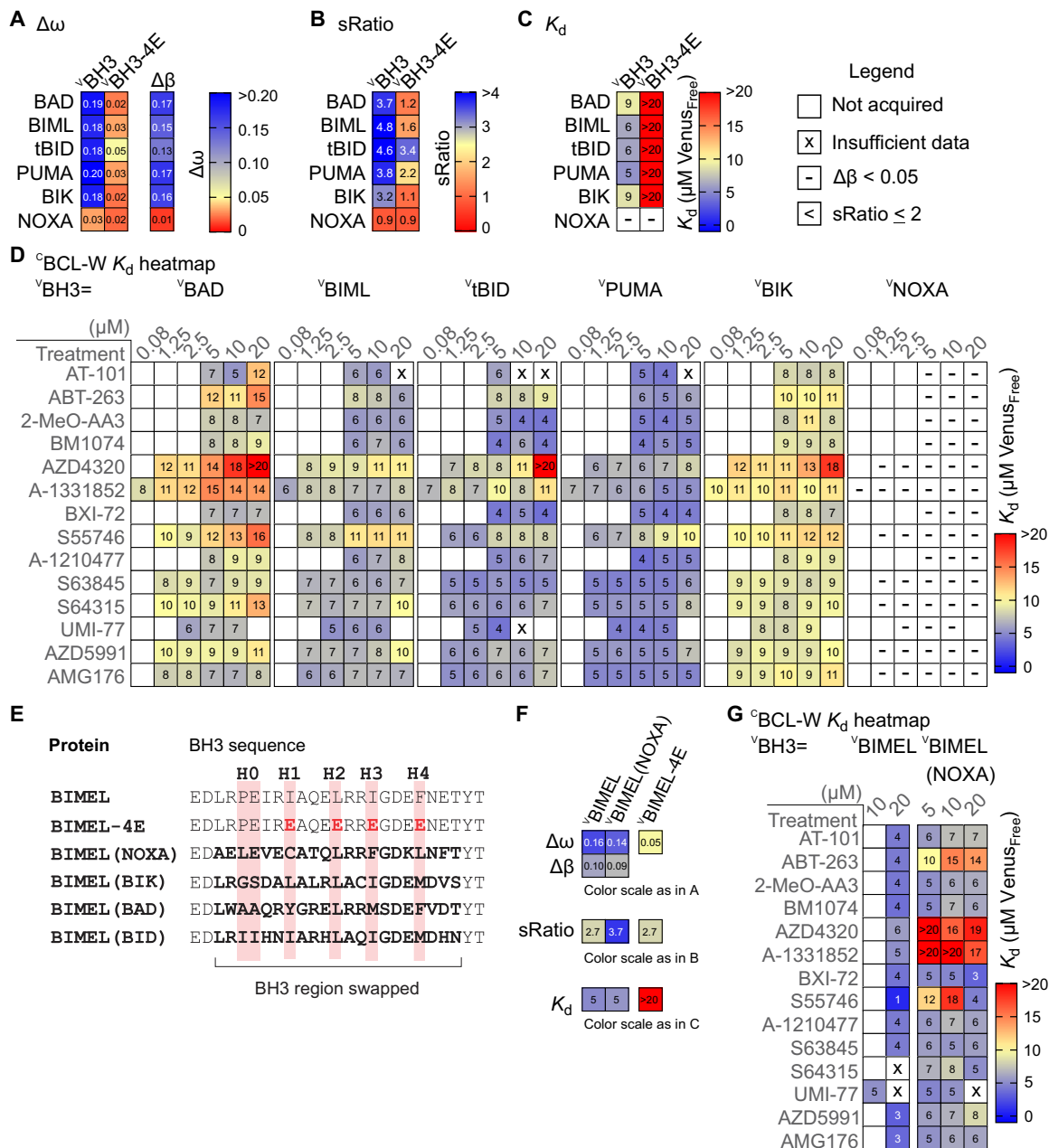


**Fig. 5. BH3 mimetic inhibition of  ${}^v\text{BH3}$  protein binding to  ${}^c\text{BCL-W}$  measured by  $qF^3$ .** (A to C) Binding of  ${}^v\text{BH3}$  proteins to  ${}^c\text{BCL-W}$  measured by  $qF^3$  as in Fig. 3. (A) Values for  $\Delta\omega$  and  $\Delta\beta$  for  ${}^c\text{BCL-W}$  binding to the individual  ${}^v\text{BH3}$  and  ${}^v\text{BH3-4E}$  control proteins. (B) sRatio values for the  ${}^v\text{BH3}$  binding to  ${}^c\text{BCL-W}$ . (C) Apparent  $K_d$ 's for the binding interactions in micromolar. For  ${}^v\text{NOXA}$ ,  $\Delta\beta < 0.05$ ; therefore,  $K_d$  was not calculated (-). Values greater than 20 are for binding data that did not saturate (sRatio < 2). (D) Heatmap of apparent  $K_d$  values for  ${}^v\text{BH3}$  proteins (listed on top) treated with BH3 mimetics (left) at concentrations indicated above each column. Insufficient binding ( $\Delta\beta < 0.05$ ) is represented as “-” in the heatmap. (E) Sequences of BH3-swap mutants. The sequence swapped in to replace the BH3 region of BIMEL is shown in bold (black). Hydrophobic residues (H0 to H4), which are key to BH3 binding antiapoptotic proteins, are highlighted in pink. The BH3 coding region of NOXA was swapped into the corresponding coding region for  ${}^v\text{BIMEL}$  to make the mutant:  ${}^v\text{BIMEL(NOXA)}$ . (F and G) The effect of all of the BH3 mimetics on the apparent  $K_d$ 's for the interaction of  ${}^v\text{BIMEL(NOXA)}$  with  ${}^c\text{BCL-W}$ , summarized from four biological replicates, is shown. (F) Controls indicate sufficient  ${}^c\text{BCL-W}:$  ${}^v\text{BIMEL(NOXA)}$  binding ( $\Delta\beta > 0.05$ ) and curve saturation (sRatio > 2) for analysis. (G) The calculated apparent  $K_d$  values in the presence of the indicated concentrations of the BH3 mimetics.

while the BCL-2/BCL-XL dual inhibitor AZD4320 (19) inhibited binding of  ${}^c\text{BCL-W}$  to  ${}^v\text{BAD}$ ,  ${}^v\text{tBID}$ , and  ${}^v\text{BIK}$ . BCL-XL inhibitor A-1331852 (14) inhibited the binding of  ${}^c\text{BCL-W}$  to both  ${}^v\text{BAD}$  and  ${}^v\text{tBID}$  and marginally to  ${}^v\text{BIK}$  (Fig. 5D). In contrast, BCL-2 inhibitor, S55746, inhibited binding of  ${}^c\text{BCL-W}$  to  ${}^v\text{BAD}$  with barely detectable effects on  ${}^v\text{BIM}$  and  ${}^v\text{BIK}$ . A small reduction

in the interaction between  ${}^c\text{BCL-W}$  and  ${}^v\text{BAD}$  was the first evidence of any potential off-target effect for the MCL-1 inhibitor, S64315.

Insufficient detected binding ( $\Delta\beta < 0.05$ ) by  $qF^3$  does not necessarily mean that two proteins do not bind. Considering the small size of NOXA relative to other BH3 proteins (Fig. 1A), we hypothesized

that NOXA positions Venus too far from the mCerulean3 on BCL-W for FRET to occur. Given the detected binding of  $^V$ BIMEL to  $^C$ BCL-W, we know that Venus can undergo FRET with mCerulean3 in this context. Therefore, to test the hypothesis, we constructed a plasmid in which the coding sequence for the NOXA BH3 sequence replaced that of  $^V$ BIMEL (Fig. 5E). Binding of the resulting BH3-swap mutant,  $^V$ BIMEL(NOXA), to  $^C$ BCL-W was readily detected by FRET (Fig. 5F and see fig. S5F for curve data), suggesting that the lack of detectable FRET between full-length  $^V$ NOXA and  $^C$ BCL-W was due to distance constraints. As expected, the binding of  $^V$ BIMEL to  $^C$ BCL-W was resistant to all of the inhibitors tested (Fig. 5G). In contrast, the binding of  $^V$ BIMEL(NOXA) to  $^C$ BCL-W was inhibited by ABT-263, AZD4320, A-1331852, and S55746, suggesting that, in cells, the affinity of NOXA for BCL-W is low.

### Assaying BH3 mimetics by measuring relocalization of $^C$ BCL-W

We took advantage of the observation that BH3 protein binding to BCL-W has been correlated with relocalization to membranes (46)

to extend some of our  $qF^3$  results. In untreated BMK-DKO cells,  $^C$ BCL-W is mainly cytoplasmic with a small fraction targeted to mitochondria (Fig. 6A). As expected, the addition of functional BH3 mimetics resulted in an increase in the relocalization of  $^C$ BCL-W from the cytoplasm to mitochondria. For example,  $<1 \mu M$  AZD4320 or A-1331852 and  $\sim 10 \mu M$  ABT-263 or S55746 resulted in a change in Pearson's  $r$  with the mitochondrial marker from  $\sim 0.35$  to 0.6, indicative of relocalization of  $^C$ BCL-W to mitochondria (Fig. 6B). As expected, no change in  $^C$ BCL-W localization was observed with  $^C$ MCL-1 inhibitors or with the inhibitors 2-MeO-AA3, BM1074, or BXI-72 determined above by  $qF^3$  to be nonfunctional. These results suggest a similar rank of  $^C$ BCL-W relocalization and drug inhibition of binding for  $^C$ BCL-W binding to  $^V$ BAD, as observed with  $qF^3$ . However,  $^C$ BCL-W relocalization did not correlate with inhibition of binding for the other  $^V$ BH3 proteins measured by  $qF^3$  and was particularly misleading for BIM and PUMA. Relocalization was also uninformative for the effects of drugs on  $^C$ BCL-2 and  $^C$ BCL-XL. Thus, unlike  $qF^3$ , relocalization did not reveal the effects of drugs on individual  $^V$ BH3 proteins binding to these antiapoptotic proteins.

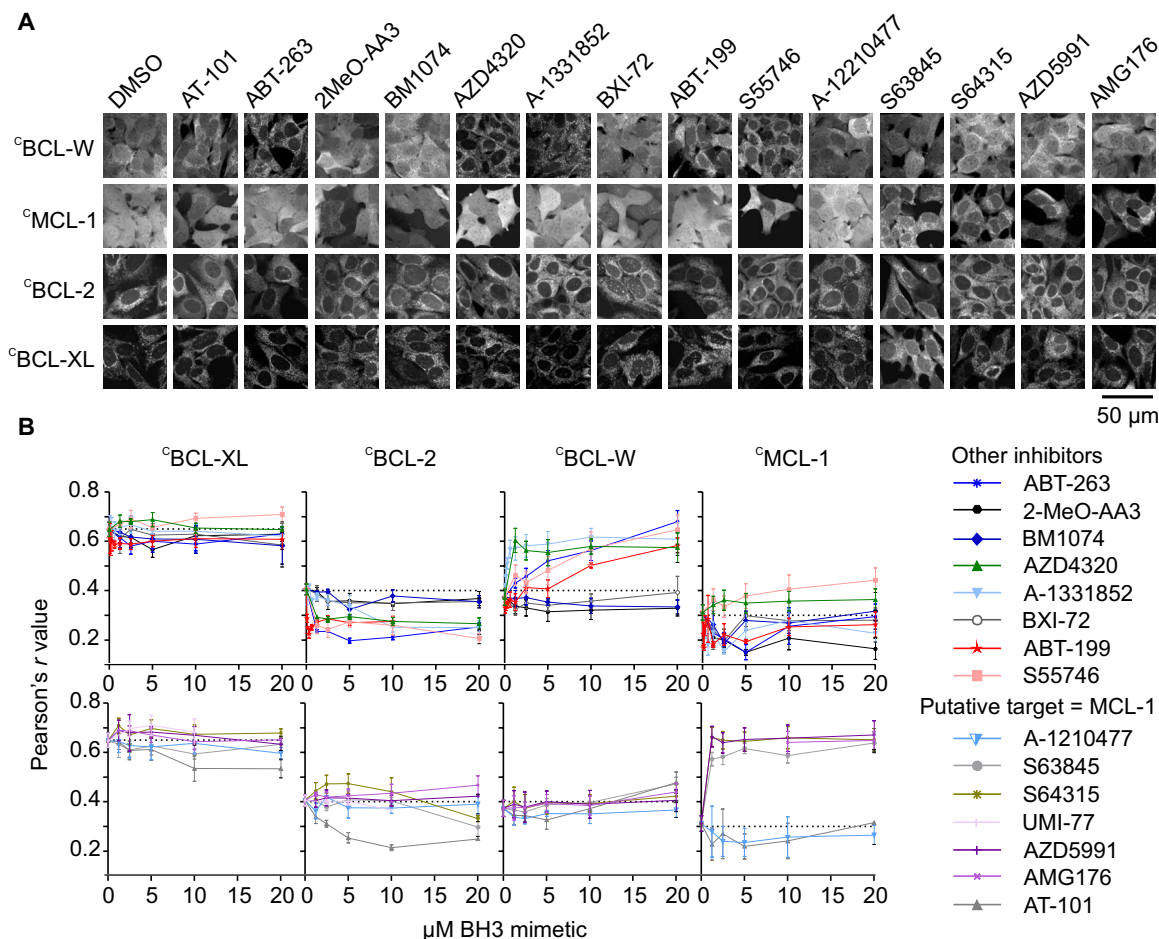


**Fig. 6. Localization of  $^C$ MCL-1 and  $^C$ BCL-W to mitochondria in response to BH3 mimetics.** (A) Example micrographs of the mCerulean3 fusion proteins acquired on the Opera Phenix automated spinning disc confocal microscope (PerkinElmer). (B) Pearson's correlation for MitoTracker Red and mCerulean3 fusion proteins (indicated above the panels) expressed in BMK-DKO cells and treated with BH3 mimetics (listed to the right). Increased mitochondrial localization at the indicated concentrations of BH3 mimetics (0.8 to 20  $\mu M$ ) results in increased Pearson's correlation (displayed here as mean and SEM from three independent replicates, with greater than 500 cells imaged per replicate). Some drugs resulted in reduced localization at mitochondria (e.g., BCL-2; presumably due to known partial localization at endoplasmic reticulum). For visualization, graphs were split by the putative target of the BH3 mimetic as indicated.

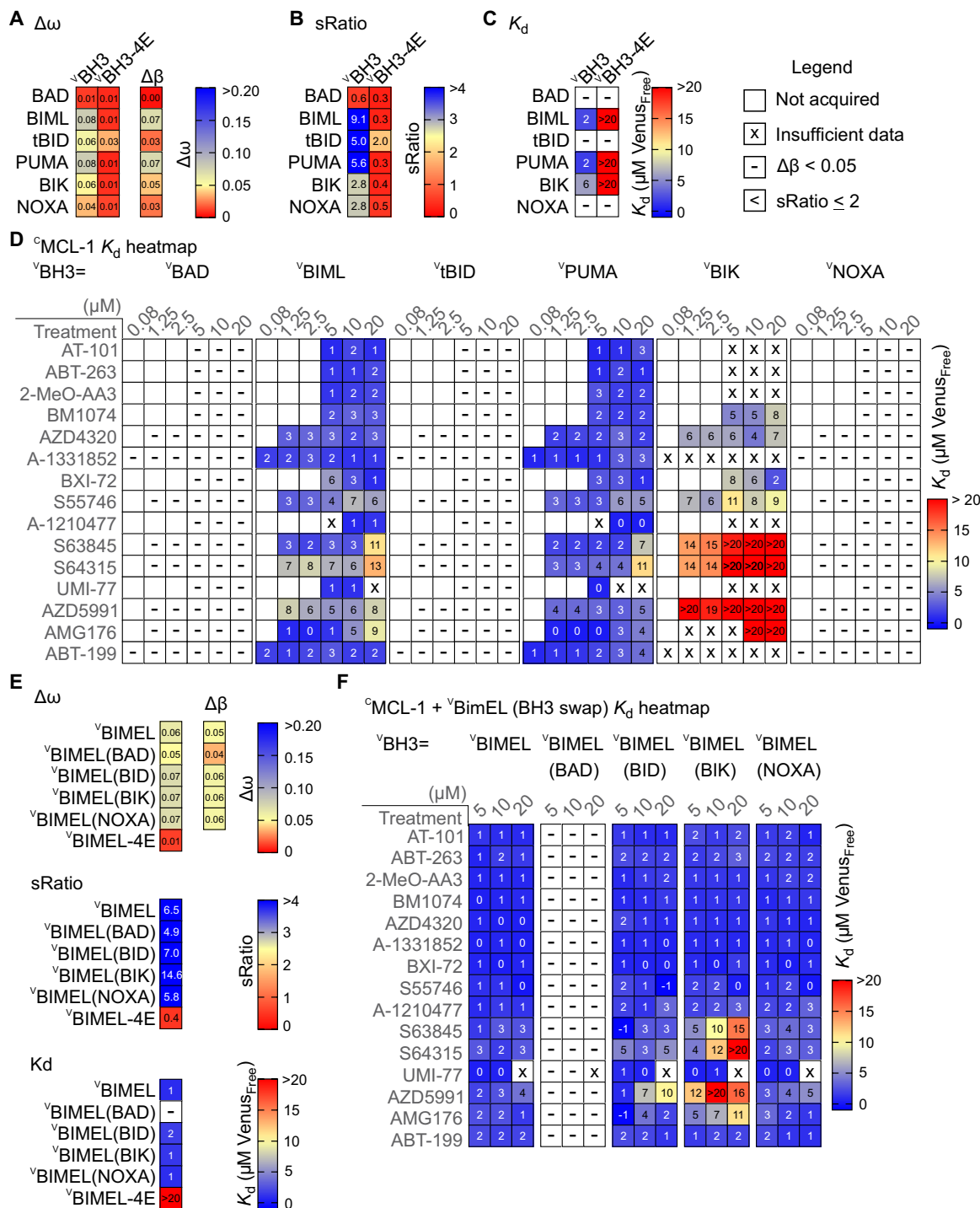


**Fig. 7. BH3 mimetic inhibition of  $\nu\text{BH3}$  protein binding to  $\text{C}^{\text{MCL-1}}$  measured by  $\text{qF}^3$ .** (A to C) Binding of  $\nu\text{BH3}$  proteins to  $\text{C}^{\text{MCL-1}}$  measured by  $\text{qF}^3$  as in Fig. 3. (A) Values for  $\Delta\omega$  and  $\Delta\beta$  for  $\text{C}^{\text{MCL-1}}$  binding to the individual  $\nu\text{BH3}$  and  $\nu\text{BH3-4E}$  control proteins. (B) sRatio values for the  $\nu\text{BH3}$  binding to  $\text{C}^{\text{MCL-1}}$ . (C) Apparent  $K_d$ 's for the binding interactions in micromolar. For  $\nu\text{BAD}$ ,  $\nu\text{tBID}$ , and  $\nu\text{NOXA}$ ,  $\Delta\beta < 0.05$ ; therefore,  $K_d$  was not calculated (-). Values greater than 20 are for binding data that did not saturate (sRatio < 2). (D) Heatmap of apparent  $K_d$  values for  $\nu\text{BH3}$  proteins (listed on top) treated with BH3 mimetics (left, gray) at concentrations indicated above each column. Insufficient binding ( $\Delta\beta < 0.05$ ) is represented as "-" in the heatmap. (E and F) To examine whether the BH3 domains of BAD, tBID, BIK, and NOXA bind to MCL-1, expression plasmids were constructed in which the BH3 coding regions were swapped into the corresponding coding region for  $\nu\text{BIMEL}$  as in Fig. 5E. Using these constructs, we analyzed the effect of each BH3 mimetic on the apparent  $K_d$ 's for the interactions. (E) Controls indicate, similar to  $\nu\text{BIMEL}$ , the BH3 domain-swapped  $\nu\text{BIMEL}$  mutants, except for  $\nu\text{BIMEL(BAD)}$ , bound to  $\text{C}^{\text{MCL-1}}$  as indicated by ( $\Delta\beta > 0.05$  and sRatio > 2). (F) The calculated apparent  $K_d$  values for the indicated  $\nu\text{BIMEL}$  mutants binding to MCL-1 in the presence of the indicated concentrations of the BH3 mimetics. See also figs. S1, S5, and S6.

### Efficacy and selectivity of inhibitors of <sup>V</sup>BH3 binding to <sup>C</sup>MCL-1

Compared with <sup>C</sup>BCL-XL, <sup>C</sup>BCL-2, or <sup>C</sup>BCL-W, less FRET was recorded for all <sup>C</sup>MCL-1 interactions (Fig. 7, A to C). Only <sup>V</sup>BIM, <sup>V</sup>PUMA, and <sup>V</sup>BIK passed criteria for calculating apparent  $K_d$ 's, and for <sup>V</sup>BIK,  $\Delta\beta$  was sufficient in only one of three biological replicates (Fig. 7D and see fig. S5A for curve data). Nevertheless, the analyzable binding data confirmed that S64315, S63845, AZD5991, AMG176, and S55746 inhibited <sup>C</sup>MCL-1 while AT-101, UMI-77, and A-1210477 did not. Furthermore, and as expected, none of the inhibitors of BCL-2, BCL-XL, and/or BCL-W inhibited <sup>C</sup>MCL-1.

MCL-1 has a longer N terminus than other antiapoptotic proteins (Fig. 1A), which may position the donor in an unfavorable position for FRET particularly with NOXA (the smallest BH3 protein) and BID and BIK as well. To further examine binding to <sup>C</sup>MCL-1, we took the same approach as for NOXA binding to <sup>C</sup>BCL-W and exchanged the BH3 region of <sup>V</sup>BIMEL with the corresponding regions of BAD, NOXA, BID, or BIK (Fig. 5E). As expected (47), <sup>C</sup>MCL-1 did not bind <sup>V</sup>BIMEL-4E or <sup>V</sup>BIMEL(BAD), while <sup>V</sup>BIMEL, <sup>V</sup>BIMEL(NOXA), <sup>V</sup>BIMEL(BID), and <sup>V</sup>BIMEL(BIK) passed the criteria for automated  $qF^3$  [Fig. 7 (E and F) and see fig. S5F for curves]. Control  $qF^3$  experiments revealed that for binding to <sup>C</sup>MCL-1, <sup>V</sup>BIMEL is more resistant than <sup>V</sup>BIML to displacement by BH3 mimetics. Consistent with this, <sup>V</sup>BIMEL(BIK) bound more tightly than <sup>V</sup>BIK to <sup>C</sup>MCL-1, but the interaction remained inhibitable by some compounds. Collectively, these results suggest that the <sup>V</sup>BIMEL BH3-swap mutants are acceptable surrogates for assaying the functional properties of BH3 mimetics. Unexpectedly, inhibition of <sup>V</sup>BIMEL(NOXA) binding to <sup>C</sup>MCL-1 was barely detectable, suggesting that unlike results with purified proteins, in cells, NOXA binding to MCL-1 may be resistant to BH3 mimetic displacement. This result suggests that the observed *in vivo* efficacy of MCL-1 inhibitors is due to the displacement of other proteins from MCL-1.

The BH3 mimetic, ABT-199, is included in Fig. 7D but not in Figs. 3 to 5. ABT-199 decreases the lifetime of the mCerulean3 donor fused to BCL-2, BCL-XL, and BCL-W but not MCL-1 (fig. S6, A and B). The absorption spectrum of ABT-199 (venetoclax) overlaps the excitation spectrum of mCerulean3; therefore, it is likely that the drug functions as a FRET acceptor (fig. S6C). As a result, ABT-199 failed criteria for screening by  $qF^3$  for BCL-2, BCL-XL, and BCL-W (see the "Quality control: Drug effect on donor lifetime" section). However, since ABT-199 did not affect the fluorescence lifetime of <sup>C</sup>MCL-1 (likely because it does not bind to the protein), it was possible to show that ABT-199 did not affect <sup>V</sup>BH3 protein binding to <sup>C</sup>MCL-1 by  $qF^3$  (Fig. 7D).

### Assaying BH3 mimetics by measuring relocalization of <sup>C</sup>MCL-1

NOXA binding to MCL-1 has been correlated with the relocalization of <sup>C</sup>MCL-1 from the cytoplasm to mitochondria (48). Consistent with our  $qF^3$  results, treatment of cells with S63845, S64315, AMG176, and AZD5991 resulted in a redistribution of <sup>C</sup>MCL-1 from the cytoplasm to mitochondria, whereas AT-101 and A-1210477 did not (Fig. 6, A and B). However, similar to the results with BCL-W earlier, drug binding was not predictive of the inhibition of the binding for individual <sup>V</sup>BH3 proteins since both BH3 protein and drug binding result in relocalization of MCL-1. Moreover, unlike the  $qF^3$  data, when assessed by relocalization, the BCL-2/BCL-XL inhibitor AZD4320 and the BCL-2 inhibitor S55746 both scored as

affecting MCL-1 localization, probably because of indirect effects. Furthermore, relocalization cannot be used to quantify the effects of drugs on individual <sup>V</sup>BH3 proteins binding to MCL-1. Thus, our  $qF^3$ -based measurements not only provided previously unknown insights into the binding of BH3 proteins to MCL-1 but also revealed unexpected drug-induced changes in the affinities of these binding interactions.

### DISCUSSION

Assessing protein-protein interactions and the effects of drugs designed to inhibit them requires an assay that recapitulates the environmental conditions of the native proteins as closely as possible. Unlike biochemical assays, measurements in live cells inherently incorporate effects related to competition from other binding partners, subcellular localization, protein turnover, drug penetration into cells, and metabolism. Our  $qF^3$  method enabled quantification of drug efficacy, affinity, and selectivity in live cells, something not previously possible for either the proteins or the drugs studied here. We examined a concentration range of 1 to 3  $\mu$ M antiapoptotic protein, which realistically approximates concentrations at mitochondria in cancer cell lines and in primary patient cells (36, 49, 50). The reported concentrations (ranging from nanomolar up to 10  $\mu$ M in colorectal tissue) are for the whole-cell volume (36, 50) and underestimate the local concentrations of these proteins at membranes (37). Although the expression levels of the antiapoptotic proteins were reasonably similar to what would be expected in cells, binding curve saturation required overexpression of the <sup>V</sup>BH3 proteins. The extent to which these proteins were overexpressed is not known as the physiological concentrations of BH3-only proteins: BAD, tBID, BIML, PUMA, NOXA, or BIK have not been reported previously. While high concentrations (up to 43  $\mu$ M <sup>V</sup>BH3 detected) were required to ensure binding curve saturation, the apparent  $K_d$ 's were at low micromolar concentrations. Nevertheless, previously reported  $K_d$  values for the binding of purified full-length BH3-only proteins to antiapoptotic proteins are lower still. For example, in the presence of membranes, full-length BCL-XL binds to tBID with a  $K_d \sim 3$  nM and BAD with  $K_d \sim 25$  nM (51). Furthermore, 20 nM purified tBID or 3 nM BIML is sufficient to induce cytochrome C release from isolated mitochondria in the presence of 100 nM BAX, which can be fully inhibited by adding 100 nM BCL-XL (5, 52). Given the high affinities of these interactions and that cells express antiapoptotic proteins at micromolar levels (36), to promote apoptosis, cellular BH3-only protein concentrations in the micromolar range are required to overcome antiapoptotic inhibition in cells. In our measured  $qF^3$  binding curves, saturation usually occurs at  $\sim 10$  to 20  $\mu$ M <sup>V</sup>BH3 (Venus<sub>Free</sub>), as expected for a donor concentration of 1 to 3  $\mu$ M. Furthermore, to enable comparisons, our calculation of Venus<sub>Free</sub> required the assumption that all interactions are heterodimeric, which may not always be the case (51).

The "apparent"  $K_d$ 's reported here depended on the concentration range of the donor analyzed and are quite different from those measured for purified proteins (fig. S3, H and I). The former result indicates that the local cellular concentration was above the absolute  $K_d$ . This is known as the "titration regime" [reviewed (35)] and is unavoidable for techniques such as isothermal calorimetry that require high protein concentrations to obtain sufficient signal. In our measurements, the phenomenon results from the expression level of the donor, which, while it is similar to that found in cancer



cells (36), is higher than the absolute  $K_d$ . In the titration regime, the apparent  $K_d$  is related to the concentration of  $Venus_{Free}$  at which half the mCerulean3 donor protein is in the bound state (35). In live cells, this apparent  $K_d$  is determined not only by the donor concentration but also by additional physiological parameters including competitive binding interactions from the unknown quantities of other potential binding partners.

In contrast to these caveats, a benefit of the  $qF^3$  technique is that the sample is equilibrated over a relatively long period (proteins expressed in cells and treated with inhibitor ~12 hours before imaging), thereby eliminating effects due to lack of sufficient equilibration before measuring an apparent  $K_d$  (35). Nevertheless, in the titration regime (35),  $qF^3$  can underestimate the relative difference in BCL-2 family binding affinities since making measurements above the  $K_d$  reduces the differences detected between strong and weak binding compared to measurements below the  $K_d$  that are described by the binding regime (35).

As a compromise that enabled examining biologically relevant concentrations and that reduced concentration-dependent differences due to varying expression levels of the various mCerulean3-antiapoptotic protein fusions, we applied a 1 to 3  $\mu M$  mCerulean3 filter to the raw binding curve data. Hence, the resulting apparent  $K_d$  values for most of the antiapoptotic-BH3 protein pairs were 3 to 4  $\mu M$ . In this way, the effects of the BH3 mimetics on inhibiting interactions were examined against a common starting point for most of the protein complexes.

Nevertheless, substantive differences in the apparent affinities were detected for a few complexes. For example, at 1 to 3  $\mu M$   $^C$ BCL-2, the apparent  $K_d$  of  $^V$ NOXA binding was 8  $\mu M$ , suggesting that  $^V$ NOXA has a lower affinity than other BH3 proteins for  $^C$ BCL-2 (Fig. 3). The lower affinity of the  $^V$ NOXA- $^C$ BCL-2 interaction was also reflected in the screen results, as lower concentrations of BH3 mimetics were required to displace  $^V$ NOXA from  $^C$ BCL-2 (Fig. 3D). Thus,  $qF^3$  can be used to estimate an apparent  $K_d$  in live cells that is closer to the absolute value for those protein-protein interactions with micromolar affinities such as  $^V$ NOXA binding to  $^C$ BCL-2. Moreover, the apparent  $K_d$  values measured in the titration regime represent relative binding affinities in the live cell environment that can be repeated consistently using similar samples by applying the same filter settings in the analysis. In general, apparent  $K_d$ 's are most useful as a quantitative readout for measuring the effect of added inhibitors, or point mutations, to an existing interaction rather than to compare affinities between different interacting partners with submicromolar absolute  $K_d$ 's. Thus, determination of whether a particular measurement conforms to the titration or binding regime is important when measuring protein-protein interactions by  $qF^3$ , as it has an impact on how the data should be interpreted. Fortunately, the determination can be made by simply testing the concentration dependence of the apparent  $K_d$  measured by  $qF^3$  (fig. S3, H and I).

Our titration regime measurements of apparent  $K_d$ 's unambiguously and quantitatively discriminate between direct and indirect effects of BH3 mimetics that, in cells, are major contributors to misidentification of BH3 mimetics in drug discovery (53). Thus, although imperfect,  $qF^3$  more closely reflects the in vivo situation than assays based on permeabilized cells, isolated mitochondria, and/or purified proteins. Moreover, using this approach, it was possible to detect binding of NOXA to BCL-2 in BMK-DKO cells, an interaction previously only controversially reported for lymphoid cells (44)

and not quantified. We also detected binding of  $^V$ NOXA to  $^C$ BCL-XL and of the NOXA BH3 region to  $^C$ BCL-W and  $^C$ MCL-1 by replacing the BH3 region of BIMEL with the NOXA BH3 region. The analysis of these mutants enabled a direct comparison of drug effects across all protein pairs. Unexpectedly, none of the MCL-1 inhibitors displaced BIMEL with the NOXA BH3 region from MCL-1, suggesting that NOXA binds very tightly to MCL-1 and that the interaction may only be terminated by protein turnover. All binding curve data are publicly available (Table 2); examples of some of the more difficult to measure pairs and their negative controls are provided in fig. S5.

Another approach that has been used to examine the binding of BH3 proteins and BH3 mimetics to anti-apoptosis proteins is the effect that these binding interactions have on the localization of the antiapoptotic proteins. The binding of the inhibitors resulted in the relocalization of  $^C$ BCL-W and  $^C$ MCL-1 but not  $^C$ BCL-XL from the cytoplasm to membranes (Fig. 6). However, for  $^C$ BCL-W and  $^C$ MCL-1, there was no correlation between compound binding and displacement of  $^V$ BH3 proteins. Structural studies of BCL-XL and almost full-length BCL-W recombinant proteins purified in the absence of detergents suggest that the C-terminal regions of these antiapoptotic proteins compete with BH3 protein binding to the soluble form of the protein (54, 55) and block low-affinity binding to the hydrophobic pocket (54). Therefore, we speculate that differences in competition between the tail and the BH3 mimetics may explain the relocalization of  $^C$ BCL-W but not  $^C$ BCL-XL. In addition, since both BH3 mimetic and BH3 protein binding result in localization at membranes, this approach is of limited utility for assessing displacement of BH3 proteins by BH3 mimetics.

Rapid protein binding measurements in live cells by  $qF^3$  enable other types of future analyses. If the off-rate of a BH3 protein-antiapoptotic complex is sufficiently low, then BH3 mimetics will function primarily by preventing complex formation rather than by displacing preexisting complexes. As a result, the induction of apoptosis by a BH3 mimetic will be determined by the rate of synthesis of new BH3 proteins and by the turnover of existing complexes. Our present data do not provide insight into the relative contributions of these factors. These measurements can be made from  $qF^3$  time-course data and extended modeling, both currently underway. Moreover, drug effects on protein-protein interactions can be studied in virtually any cell type using  $qF^3$ . Thus, it will be possible to address cell type-specific changes in the efficacy and selectivity of BH3 mimetics due to differences in the expression of endogenous proteins and posttranslational modifications in different cell types. The binding of BH3 proteins to antiapoptotic proteins and the effects of BH3 mimetics are currently being examined in neurons.

Our  $qF^3$  data confirmed much of what was already known about some of the inhibitors: ABT-263 inhibited BCL-2 and BCL-XL, while A-1331852 inhibited BCL-XL but not BCL-2 (26); MCL-1 did not bind BAD, and MCL-1 inhibitors generally did not inhibit BCL-2, BCL-XL, or BCL-W. However, beyond these observations, many results were unexpected: None of the drugs tested inhibited PUMA binding to BCL-2 or BCL-W, and only A-1331852 marginally reduced PUMA binding to BCL-XL. Similarly, only the highest concentration (20  $\mu M$ ) of S64315 or S63845 reduced PUMA binding to MCL-1. As PUMA is a major contributor to the regulation of cell death in neurons (56), the relative paucity of inhibition revealed here may explain why undesirable on-target neurodegeneration has not been reported for BH3 mimetics in preclinical and clinical studies to date. Furthermore,  $qF^3$  revealed seven unexpected results



**Table 2. List of key resources.** List of source and identifier for reagents and resources used here. Links to all uploaded data, software, and custom-written scripts are listed. NA, not applicable; PBS, phosphate-buffered saline; 3D, three dimensions; NMR, nuclear magnetic resonance; PDB, Protein Data Bank; HEK, human embryonic kidney.

Reagent or resource	Source	Identifier
<b>Antibodies</b>		
GFP (4B10) Mouse mAb	Cell Signaling Technologies	Catalog no. 29555, RRID:AB_1196614
GAPDH (14C10) Rabbit mAb	Cell Signaling Technologies	Catalog no. 2118S, RRID:AB_561053
Peroxidase AffiniPure Donkey Anti-Mouse IgG (H+L)	Jackson ImmunoResearch Laboratories	Catalog no. 715-035-150, RRID:AB_2340770
Peroxidase AffiniPure Donkey Anti-Rabbit IgG (H+L)	Jackson ImmunoResearch Laboratories	Catalog no. 711-035-152, RRID:AB_10015282
<b>Bacterial and virus strains</b>		
BL21-AI One Shot Chemically Competent <i>E. coli</i>	Thermo Fisher Scientific	Catalog no. C607003
<b>Biological samples</b>		
Annexin V protein labeled with Alexa Fluor 488 (Life Technologies, catalog no. A20000; Alexa Fluor succinimidyl ester)	Produced in-house. Purified from bacteria and labeled with fluorescent dye. PMID: 18314054. Our labeled protein stocks are 0.3 mg/ml.	NA
<b>Chemicals, peptides, and recombinant proteins</b>		
mCerulean3 purified protein	This paper. Produced in-house.	See DOI: 10.21203/rs.3.pex-1354/v1
Venus purified protein	This paper. Produced in-house.	See DOI: 10.21203/rs.3.pex-1354/v1
Tetramethylrhodamine ethyl ester	Thermo Fisher Scientific	Catalog no. T669
DRAQ5	BioStatus	Catalog no. DR05500
MitoTracker Red	Thermo Fisher Scientific	Catalog no. M22425
MitoTracker Green	Thermo Fisher Scientific	Catalog no. M7514
Fluorescein	Sigma-Aldrich	Catalog no. F6377-100G
Gibco Trypsin-EDTA (0.5%), no phenol red (diluted 1 in 5 in PBS)	Fisher Scientific	Catalog no. 15-400-054
PBS, autoclaved	Made in-house, standard recipe	NA
Chymostatin	Sigma-Aldrich	Catalog no. C7268
Antipain	Sigma-Aldrich	Catalog no. A6191
Leupeptin	Sigma-Aldrich	Catalog no. L2884
Pepstatin	Sigma-Aldrich	Catalog no. P5318
Aprotinin	Sigma-Aldrich	Catalog no. 10820
Phenylmethylsulfonyl fluoride	BioShop	Catalog no. PMS123.25
L-(+)-Arabinose	BioShop	Catalog no. ARB222.500
Actinomycin D	Sigma-Aldrich	Catalog no. A4262
Gibco MEM $\alpha$ , no nucleosides, powder	Fisher Scientific	Catalog no. 12000022
Gibco DMEM high glucose, powder	Fisher Scientific	Catalog no. 12100061
Fetal bovine serum	Sigma-Aldrich	Catalog no. F1051
Penicillin-streptomycin	Fisher Scientific	Catalog no. 15-140-122
100X MEM Non-Essential Amino Acids	Gibco	Catalog no. 11140076
Ni-NTA Agarose	Invitrogen	Catalog no. R901-15
Ampicillin	BioShop	Catalog no. 69-52-3
Anhydrous DMSO	Fisher Scientific	Catalog no. BP231-100
AT-101 also named "(–)-Gossypol"	Selleck Chemicals	Catalog no. S2812
ABT-263 also named "navitoclax"	ChemieTek	Catalog no. CT-A263
2-MeO-AA3 also named "2-meoxy-antimycin A3"	Abcam	Catalog no. ab141523
BM1074	Cedarlane	Catalog no. B595855

continued on next page

Reagent or resource	Source	Identifier
AZD4320	ChemieTek	Catalog no. CT-A4320
A-1331852	Selleck Chemicals	Catalog no. S8759
BXI-72 also named, "bisbenzimidazole H33258"	Sigma-Aldrich	Catalog no. 23491-45-4
ABT-199 also named "venetoclax" and "Venclexta"	ChemieTek	Catalog no. CT-A199
S55746 also named "BCL-201"	Selleck Chemicals	Catalog no. S58759
A-1210477	Selleck Chemicals	Catalog no. S7790
S63845	ChemieTek	Catalog no. CT-S63845
S64315 also named "MIK665"	ChemieTek	Catalog no. CT-MIK665
UMI-77	Sigma-Aldrich	Catalog no. SML1492
AZD5991	ChemieTek	Catalog no. CT-A5991
AMG176	ChemieTek	Catalog no. CT-AMG176
<b>Critical commercial assays</b>		
GeneJET Plasmid Midiprep Kit	Thermo Fisher Scientific	Catalog no. K0481
TransIT-X2 Transfection Reagent	Mirus	Catalog no. Mir 6003
<b>Deposited data</b>		
Figure 3, combined binned binding curve data for four replicates of two screens. Final results of $qF^3$ analysis are summarized in heatmaps.	This paper; Dataverse	<a href="https://doi.org/10.5683/SP2/AYZ2T0">https://doi.org/10.5683/SP2/AYZ2T0</a>
Figure 3, for each square in heatmaps, see corresponding fit and combined binned data plotted with positive and negative controls.	This paper; Dataverse	<a href="https://doi.org/10.5683/SP2/ONHXZZ">https://doi.org/10.5683/SP2/ONHXZZ</a>
Figure 4, combined binned binding curve data for four replicates of two screens. Final results of $qF^3$ analysis are summarized in heatmaps.	This paper; Dataverse	<a href="https://doi.org/10.5683/SP2/QN9C9R">https://doi.org/10.5683/SP2/QN9C9R</a>
Figure 4, for each square in heatmaps, see corresponding fit and combined binned data plotted with positive and negative controls.	This paper; Dataverse	<a href="https://doi.org/10.5683/SP2/NZJBCJ">https://doi.org/10.5683/SP2/NZJBCJ</a>
Figure 5, combined binned binding curve data for four replicates of two screens. Final results of $qF^3$ analysis are summarized in heatmaps.	This paper; Dataverse	<a href="https://doi.org/10.5683/SP2/RZXEZZ">https://doi.org/10.5683/SP2/RZXEZZ</a>
Figure 5, for each square in heatmaps, see corresponding fit and combined binned data plotted with positive and negative controls.	This paper; Dataverse	<a href="https://doi.org/10.5683/SP2/YLHF73">https://doi.org/10.5683/SP2/YLHF73</a>
Figure 6, example raw image data. Colocalization analysis results for four independent replicates. As an additional resource, refer to the description on Dataverse for a link to all original images.	This paper; Dataverse	<a href="https://doi.org/10.5683/SP2/05HJNT">https://doi.org/10.5683/SP2/05HJNT</a>
Figure 7, combined binned binding curve data for four replicates of two screens. Final results of $qF^3$ analysis are summarized in heatmaps.	This paper; Dataverse	<a href="https://doi.org/10.5683/SP2/F3KQCV">https://doi.org/10.5683/SP2/F3KQCV</a>
Figure 7, for each square in heatmaps, see corresponding fit and combined binned data plotted with positive and negative controls.	This paper; Dataverse	<a href="https://doi.org/10.5683/SP2/2VMFFL">https://doi.org/10.5683/SP2/2VMFFL</a>
fig. S1, raw Western blot data and analyzed cell death in multiple cell lines (3 replicates each). As an additional resource, refer to the description on Dataverse for a link to all original images.	This paper; Dataverse	<a href="https://doi.org/10.5683/SP2/FQP6VY">https://doi.org/10.5683/SP2/FQP6VY</a>
Figure S3, raw data: Coomassie gel, lifetime, and spectra for purified mCerulean3 and Venus; distribution of mCerulean3 expression in stable cell lines; and the effect of mCerulean3 filter on resulting $K_d$	This paper; Dataverse	<a href="https://doi.org/10.5683/SP2/TIPUGZ">https://doi.org/10.5683/SP2/TIPUGZ</a>
Figure S3, data used to calculate G factor.	This paper; Dataverse	<a href="https://doi.org/10.5683/SP2/IEZ8TI">https://doi.org/10.5683/SP2/IEZ8TI</a>

*continued on next page*

Reagent or resource	Source	Identifier
Figure S4A, raw image data	This paper; Dataverse	<a href="https://doi.org/10.5683/SP2/NDBW4K">https://doi.org/10.5683/SP2/NDBW4K</a>
Figure S4B, raw binding curve data for BCL-W:BIML interaction displayed in 3D and combined binned data for four replicates	This paper; Dataverse	<a href="https://doi.org/10.5683/SP2/PIIS0V">https://doi.org/10.5683/SP2/PIIS0V</a>
Figure S5 data including simulated and raw sRatio data; example raw binding curves for protein-protein interactions that failed to meet $\Delta\beta > 0.05$ threshold; and raw binding curves for <sup>V</sup> NOXA with <sup>C</sup> BCL-2, <sup>C</sup> BCL-W, and <sup>C</sup> MCL-1.	This paper; Dataverse	<a href="https://doi.org/10.5683/SP2/SPHV6G">https://doi.org/10.5683/SP2/SPHV6G</a>
Figure S6, raw lifetime measurements with each BH3 mimetic treatment ( $n = 3$ ) and raw spectra of ABT-199	This paper; Dataverse	<a href="https://doi.org/10.5683/SP2/BKRC8R">https://doi.org/10.5683/SP2/BKRC8R</a>
NMR structure of BCL-W	PMID: 12660157	PDB: 1O0L
qF <sup>3</sup> analysis codes	This paper; GitHub	<a href="https://github.com/DWALab/Osterlund_et_al_2021.git">https://github.com/DWALab/Osterlund_et_al_2021.git</a>
<b>Experimental models: Cell lines</b>		
MCF-7 ( <i>Homo sapiens</i> )	Gift from R. N. Buick (University of Toronto). PMID: 3790748.	NA
HEK293 or 293 cells ( <i>H. sapiens</i> )	Gift from F. Graham (McMaster University). PMID: 886304.	
BMK ( <i>M. musculus</i> )	Gift from E. White (Rutgers University). PMID: 11836241.	NA
BMK ( <i>M. musculus</i> ) with BAX and BAK double knockout (BMK-DKO or BMK-d3)	Gift from E. White (Rutgers University) PMID: 11836241.	NA
Human colon carcinoma cells, HCT116 ( <i>H. sapiens</i> )	Gift from B. Vogelstein (Johns Hopkins Kimmel Cancer Center, Baltimore, MD). PMID: 9121588.	NA
HCT116 with BAX and BAK double knockout (HCT116-DKO) ( <i>H. sapiens</i> )	Gift from B. Vogelstein (Johns Hopkins Kimmel Cancer Center, Baltimore, MD). PMID: 11062132.	NA
<b>Recombinant DNA</b>		
Plasmid: mVenus-pEGFP-C1	Gift from R. Truant (McMaster University)	Addgene plasmid no. 27794
Plasmid: mCerulean3-pEGFP-C1	Gift from M. A. Rizzo (University of Maryland)	Addgene plasmid no. 54730
Plasmid: pSPUTK	Stratagene, Santa Clara, CA	Catalog no. CB4278654
Plasmid: Venus-BAD-pEGFP-C1	PMID: 30860026	Addgene plasmid no. 166733
Plasmid: Venus-BIML-pEGFP-C1	PMID: 30860026	Addgene plasmid no. 166734
Plasmid: Venus-tBID-pEGFP-C1	PMID: 30860026	Addgene plasmid no. 166736
Plasmid: Venus-BIK-pEGFP-C1	This paper	Addgene plasmid no. 166737
Plasmid: Venus-NOXA-pEGFP-C1	This paper	Addgene plasmid no. 166738
Plasmid: Venus-PUMA-pEGFP-C1	This paper	Addgene plasmid no. 166739
Plasmid: Venus-BAD4E-pEGFP-C1	PMID: 30860026	Addgene plasmid no. 166740
Plasmid: Venus-BIML4E-pEGFP-C1	PMID: 30860026	Addgene plasmid no. 166741
Plasmid: Venus-tBID4E-pEGFP-C1	This paper	Addgene plasmid no. 166743
Plasmid: Venus-BIK4E-pEGFP-C1	This paper	Addgene plasmid no. 166744
Plasmid: Venus-NOXA4E-pEGFP-C1	This paper	Addgene plasmid no. 166745
Plasmid: Venus-PUMA4E-pEGFP-C1	This paper	Addgene plasmid no. 166746
Plasmid: Venus-tBID2E-pEGFP-C1	This paper	Addgene plasmid no. 166747
Plasmid: Venus-BAD2A-pEGFP-C1	This paper	Addgene plasmid no. 166748
Plasmid: Venus-BIMEL-pEGFP-C1	PMID: 30860026	Addgene plasmid no. 166735
Plasmid: Venus-BIMEL-4E-pEGFP-C1	PMID: 30860026	Addgene plasmid no. 166742

continued on next page

Reagent or resource	Source	Identifier
Plasmid: Venus-BIMEL(BAD)-pEGFP-C1	PMID: 30860026	Addgene plasmid no. 166758
Plasmid: Venus-BIMEL(BID)-pEGFP-C1	This paper	Addgene plasmid no. 166759
Plasmid: Venus-BIMEL(BIK)-pEGFP-C1	This paper	Addgene plasmid no. 166760
Plasmid: Venus-BIMEL(NOXA)-pEGFP-C1	This paper	Addgene plasmid no. 166761
Plasmid: mCerulean3-BCL-XL-s2193	PMID: 30860026	Addgene plasmid no. 166749
Plasmid: mCerulean3-BCL-2-s2193	PMID: 30860026	Addgene plasmid no. 166750
Plasmid: mCerulean3-BCL-W-FUGW	This paper	Addgene plasmid no. 166751
Plasmid: mCerulean3-MCL-1-pLVX	This paper	Addgene plasmid no. 166752
Plasmid: mCerulean3-5aa-Venus-pEGFP-C1	PMID: 17040988	Addgene plasmid no. 26394
Plasmid: mCerulean3-13aa-Venus-pEGFP-C1	This paper	Addgene plasmid no. 166753
Plasmid: mCerulean3-31aa-Venus-pEGFP-C1	This paper	Addgene plasmid no. 166754
Plasmid: mCerulean3-39aa-Venus-pEGFP-C1	This paper	Addgene plasmid no. 166755
Plasmid: His6-TEV-Venus-pBluescript	This paper	Addgene plasmid no. 166756
Plasmid: His6-TEV-mCerulean3-pBluescript	This paper	Addgene plasmid no. 166757
<b>Software and algorithms</b>		
MATLAB with toolboxes: Signal Processing, Curve Fitting, Image Processing	Version R2020a	<a href="http://www.mathworks.com/products/matlab.html">www.mathworks.com/products/matlab.html</a>
INO software package including INO-FHS Acquisition, INO_FHS_Analysis, and INO_FHS_Batch Analysis	INO Client Release_r10357 package	Contact lead
ImageJ	Plugin "ImageJ for microscopy" by T. Collins, McMaster University	<a href="https://imagej.nih.gov/ij/">https://imagej.nih.gov/ij/</a> and <a href="https://imagej.nih.gov/ij/plugins/mbf/index.html">https://imagej.nih.gov/ij/plugins/mbf/index.html</a>
CellProfiler	Version 2.2.0, rev ac0529e	<a href="https://cellprofiler.org/">https://cellprofiler.org/</a>
PerkinElmer Harmony Software for high-content analysis	Version 4.9	<a href="http://www.perkinelmer.com/category/image-analysis-software">www.perkinelmer.com/category/image-analysis-software</a>
GraphPad Prism	Version 8	<a href="http://www.graphpad.com/scientific-software/prism/">www.graphpad.com/scientific-software/prism/</a>
Microsoft Excel	2010	<a href="http://www.microsoft.com/">www.microsoft.com/</a>
Tecan i-Control software	Version 2.0	<a href="https://lifesciences.tecan.com/plate_readers/infinite_200_pro?p=tab-3">https://lifesciences.tecan.com/plate_readers/infinite_200_pro?p=tab-3</a>
<b>Other</b>		
Opera Phenix high-content screening system	PerkinElmer	Catalog no. HH14000000
Infinite M1000 microplate reader	Tecan	
Detailed step-by-step protocol for qF <sup>3</sup>	This paper; see associated text at Protocol Exchange: Title, "Automated, quantitative Fast FLIM-FRET (qF3): A step-by-step protocol to measure dissociation constants for protein-protein interactions in live-cell screening applications."	<a href="https://dx.doi.org/10.21203/rs.3.pex-1354/v1">https://dx.doi.org/10.21203/rs.3.pex-1354/v1</a>
Instructional videos for running qF <sup>3</sup> analysis	This paper; YouTube and linked to at GitHub	<a href="http://www.youtube.com/playlist?list=PLUiSJrzzg9v0e5sjA57olbfOLAGlrHXRC">www.youtube.com/playlist?list=PLUiSJrzzg9v0e5sjA57olbfOLAGlrHXRC</a>
qF <sup>3</sup> analysis code	This paper; Dataverse	<a href="https://doi.org/10.5683/SP3/QYDEDH">https://doi.org/10.5683/SP3/QYDEDH</a>

about drug actions in live cells: (i) The spectrum of activity of ABT-263 is different when inhibiting BCL-2 and BCL-XL. (ii) The BCL-2 inhibitor S55746 [reported 70- to 400-fold selectivity for BCL-2 over BCL-XL (17)] has off-target effects in live cells on BCL-XL that depend on the BH3 binding partner being examined. (iii) Other BH3 mimetics previously reported as inhibiting BCL-XL (13, 16, 20, 45) had no direct effect in cells. (iv) BH3 mimetics, A-1331852, S55746, and AZD4320, unexpectedly inhibited BCL-W binding to BAD and NOXA and marginally to BID and BIK. (v) Conversely, inhibition of BCL-W by ABT-263 was unexpectedly

limited to only BAD and NOXA. (vi) Inhibition of antiapoptotic protein binding to BIK was highly variable: ABT-263 inhibited only BCL-XL binding to BIK, while S55746 inhibited only BCL-2 binding to BIK, and AZD4320 inhibited BCL-2, BCL-XL, and BCL-W binding to BIK. (vii) S55746 inhibited BCL-2 binding to BID and not BIM, while the same drug inhibited BCL-XL binding to BIM and not BID.

These examples of unexpected specificities strongly suggest that adding qF<sup>3</sup> to the drug development pipeline will provide valuable data to guide medicinal chemistry efforts and improve preclinical validation of compounds, thereby providing substantial savings on

drug development. Moreover, our results indicate that it should be possible to design inhibitors that are much more specific for individual pairs of BCL-2 family proteins than previously anticipated. Such inhibitors could be designed to reduce on-target side effects while maximizing effectiveness for patient/disease-specific applications. For example, it appears that platelets require BCL-XL binding to BAD for survival (57–59). Thus, it may be possible to use qF<sup>3</sup> to guide the development of a BCL-XL inhibitor that does not disrupt this complex to selectively trigger apoptosis in cancer cells without causing the thrombocytopenia seen for inhibition of BCL-XL by ABT-263 (60). Last, qF<sup>3</sup> will also enable future studies of the mechanisms by which drug resistance is conveyed by mutation(s) of the proteins that regulate apoptosis and guide the development of next generation drugs to overcome these mechanisms of acquired resistance. Already, several mutations in BCL-2 have been associated with venetoclax resistance in lymphoma cell lines under continuous exposure (61) and in patients with chronic lymphocytic leukemia (62, 63). Thus, drug discovery efforts guided by qF<sup>3</sup> to further develop small molecules to optimize therapeutic regulation of apoptosis are only just beginning.

## MATERIALS AND METHODS

Included here is a comprehensive overview of our qF<sup>3</sup> method (summarized in fig. S4) along with the other methods used. However, we have also written a much more detailed step-by-step qF<sup>3</sup> procedure and made a video tutorial for running the analyses (see Table 2 for the link). Any further information should be directed to and will be fulfilled by the lead contact: D.W.A. (david.andrews@sri.utoronto.ca).

### Using FLIM to measure FRET for resolution of direct protein-protein interactions in live cells

Nonradiative transfer of energy can occur when a donor fluorophore and a suitable acceptor molecule with sufficient spectral overlap and dipole-dipole alignment are in close proximity, generally less than 10 nm. FRET is described by Eq. 1

$$E = \frac{1}{1 + \left(\frac{r}{R_0}\right)^6} \quad (1)$$

where  $E$  is energy transfer,  $r$  is the distance between the donor and acceptor, and  $R_0$  is the distance at which 50% energy transfer occurs. For mCerulean3 and Venus fluorescence proteins,  $R_0$  is 5.71 nm (64). The marked dependence on distance (sixth power in the denominator) makes FRET a molecular ruler with which to measure interactions between interacting proteins. FRET results in a decrease in donor emission and an increase in acceptor emission; however, fluorescence intensity is also related to the local concentrations of the fluorophores. For this reason, intensity-based measurements of FRET in images are prone to a variety of errors owing to convolution of the intensity changes due to concentration, FRET, and bleed-through between the two spectral channels (24, 65). In contrast, the time a fluorophore remains in the excited state before returning to the ground state (the fluorescence lifetime) is a physical property of the donor and is concentration independent (66). Decay to the ground state is accelerated by FRET; therefore, FLIM measurement of FRET is the gold standard method for quantifying protein-protein interactions in cells (24, 65, 67).

## DNA constructs

All plasmids used here are available from Addgene (Table 2). Plasmids for transient expression of Venus fused to full-length BH3 proteins BAD, PUMA, BIK, NOXA (human), BIML, BIMEL, or tBID (mouse) were assembled in the pEGFP-C1 plasmid backbone in which the enhanced green fluorescent protein (EGFP) coding region was replaced with that of Venus. To generate collisional controls for each protein, we mutated the BH3 region to eliminate binding (“<sup>V</sup>BH3-4E mutants”) (Fig. 2A). All plasmids were sequenced before use. Fusion proteins were demonstrated to have the expected cell death regulatory activity in cells (fig. S1, B and C). In the plasmid for <sup>V</sup>BIMEL expression, we exchanged the BH3 binding region for the BH3 sequence of BAD, NOXA, BIK (human), or BID (mouse) by polymerase chain reaction (PCR)-mediated site-directed mutagenesis. These constructs are referred to as “BH3-swap” mutants (Figs. 5, E to G, and 7, E and F), and DNA constructs are named in the following format: “V-BIMEL(BH3 region swapped in)-pEGFP-C1.”

Four constructs were used for generating stable cell lines: mCerulean3-BCL-XL-s2193, mCerulean3-BCL-2-s2193, mCerulean3-BCL-W-FUGW, and mCerulean3-MCL-1-pLVX. For genes in “s2193” backbone, we transfected BMK-DKO cells, selected with blasticidin (5 μg/ml) for 2 weeks, and then sorted for mCerulean3 expression. For genes in the FUGW and pLVX lentiviral transfer plasmid backbone we transfected human embryonic kidney (HEK) 293T cells along with psPAX2 plasmid encoding viral packaging proteins (genes Gag, Pol, Rev, Tat) and a plasmid encoding viral envelope protein: vesicular stomatitis virus glycoprotein (VSV-G). Then after 48 to 72 hours we harvested the virus and infected BMK-DKO cells. For selection, puromycin (4 μg/ml) was used to generate the BMK-DKO-<sup>C</sup>MCL-1 cell line. Antibiotic selection was unnecessary for creating our BMK-DKO-<sup>C</sup>BCL-W cell line, as viral titer was high.

Five constructs were used in determining the  $G$  factor of the National Optics Institute (INO)-FLIM hyperspectral (INO-FHS). Genes encoding proteins mCerulean3, Venus, mCerulean3-5aa-Venus (68), mCerulean3-13aa-Venus, mCerulean3-31aa-Venus, or mCerulean3-39aa-Venus (where “aa” indicates the number of amino acids in the linker between the two fluorophores) were subcloned into the “pEGFP-C1” plasmid backbone.

## Cell maintenance

All cell lines were maintained at 37°C and 5% CO<sub>2</sub> and tested for mycoplasma every 2 weeks in culture by PCR as previously described (69). BMK [gender unspecified (70)], HCT116 (human colon carcinoma; gender, male), and HEK293T (human embryonic kidney; gender, female) cells were maintained in Dulbecco’s modified Eagle’s medium [DMEM; 10% fetal bovine serum (FBS) + 1% penicillin-streptomycin + 1% MEM Non-Essential Amino Acids] and split 1 in 10 every 2 to 3 days (71, 72). MCF-7 (human breast cancer; gender, female) cells were cultured in Minimum Essential Medium Eagle - alpha modification (αMEM) media (10% FBS + 1% penicillin-streptomycin) and split 1 in 5, every 2 to 3 days (73). “DKO” indicates double knockout of BAX<sup>-/-</sup> and BAK<sup>-/-</sup> in the named cell line. MCF-7, HCT116, and HEK293T cells were authenticated at The Hospital for Sick Children facility in Toronto by short tandem repeat genotyping. HCT116 DKO (74) and BMK DKO (70) cell lines were validated by Western blot for the absence of detectable BAX and BAK compared to the parental cells. BMK cells were submitted to the American Type Culture Collection



(ATCC) for mouse short tandem repeat profiling of 18 loci. Without a reference, results could not fully authenticate BMK cell identity; however, we can confirm that our BMK cells have a murine origin and are a 90% match to ATCC's profile for murine embryonic fibroblast cell line CRL-2907. Cell lines used here do not fall on the list of commonly misidentified cell lines ([https://en.wikipedia.org/wiki/List\\_of\\_contaminated\\_cell\\_lines](https://en.wikipedia.org/wiki/List_of_contaminated_cell_lines)).

To generate stable cell lines, lentiviral expression plasmids were assembled with the coding region of mCerulean3 followed in-frame by that of BCL-XL, BCL-2, MCL-1 (human), or BCL-W (mouse). To note, there is high sequence conservation between human and mouse BCL-W: with only three amino acid changes from human to mouse [mutation A7T is in an unstructured loop, and E124D and Q133R are within helix 6 facing away from the core of the BCL-W nuclear magnetic resonance structure Protein Data Bank 1O0L (54)]. BMK-DKO<sup>C</sup>BCL-XL, BMK-DKO<sup>C</sup>BCL-2, MCF-7<sup>C</sup>BCL-XL, and MCF-7<sup>C</sup>BCL-2 cell lines were used previously (26). BMK-DKO<sup>C</sup>MCL-1 and BMK-DKO<sup>C</sup>BCL-W cell lines were made by high-titer infection with lentivirus. BMK-DKO<sup>C</sup>MCL-1 cells were grown under selection with puromycin (4 μg/ml). Any of these stable cell lines are available upon request from the lead contact.

### Image-based cell death assay

Cell death was measured as previously described (26). Briefly, data were collected on the Opera Phenix high-content screening platform (PerkinElmer) 24 hours following transfection (fig. S1, B and C) with plasmids encoding the indicated BH3 proteins or BH3 mimetic treatment (fig. S1D). Features were calculated from images of mitochondrial transmembrane potential (tetramethylrhodamine ethyl ester staining), nuclear morphology (DRAQ5 stain), and externalization of phosphatidylserine (annexin V binding) (75–77). DRAQ5 stains primarily the nucleus, but also stains enough of the cytoplasm to allow cell segmentation. Thus, cell morphology features including cell shrinkage and blebbing of the plasma membrane were also calculated and used in the analyses. Images were automatically classified as alive or dead by a linear classifier trained on at least 100 cells manually annotated by the user from micrographs of cells in positive and negative control wells in each experiment (Harmony software, PerkinElmer).

### Colocalization analyses

Cell lines expressing the mCerulean3 to antiapoptotic fusion proteins BMK-DKO<sup>C</sup>BCL-XL, BMK-DKO<sup>C</sup>BCL-W, BMK-DKO<sup>C</sup>BCL-2, and BMK-DKO<sup>C</sup>MCL-1 were seeded at 2000 cells per well in a CellCarrier-384 Ultra microplate. The following day, cells were treated with BH3 mimetics (1.25 to 20 μM) maintaining the same final concentration of DMSO (1:1000). The plate was incubated for 12 to 18 hours and stained with 5 μM DRAQ5 and 200 nM MitoTracker Red. As a positive control, 100 nM MitoTracker green was used to stain untransfected (no Venus expression) cells only. Four channels were collected on the Opera Phenix high-content screening system, and the micrographs were analyzed using CellProfiler as previously described (26). mCerulean3 (excitation, 425 nm; emission, 435 to 480 nm), DRAQ5 (excitation, 640 nm; emission, 650 to 760 nm), MitoTracker Green (excitation, 488 nm; emission, 500 to 550 nm), and MitoTracker Red (excitation, 561 nm; emission, 570 to 630 nm) channels were acquired sequentially, automatically switching between four channels at each field of view. Micrographs acquired with the ×40 water immersion objective

(numerical aperture, 1.1) are 300 μm by 300 μm in size with 1080 × 1080 pixel resolution.

Briefly, cells were segmented using the DRAQ5 nuclear channel; then, cells were filtered by size and intensity to remove any dead cells and any unstained cell that had lost stable expression of the mCerulean3 fusion protein of interest. Then, within the cytoplasmic area of the cell, Pearson's correlation was measured between mCerulean3 and MitoTracker Red channels and between MitoTracker Green and MitoTracker Red channels (positive control).

Representative images displayed in Fig. 6A are for visual inspection only and have been cropped and brightness- and contrast-adjusted equally. More than 500 cells were analyzed per replicate. Three biological replicates were acquired, and the median Pearson's *r* value of each replicate was determined. The mean and SEM of these three independent replicates are displayed in Fig. 6B.

### Immunoblotting

For the 200× protease inhibitor cocktail (PIN) recipe, add 20 μl of chymostatin (10 mg/ml in DMSO), 20 μl of antipain (10 mg/ml in DMSO), 20 μl of leupeptin (10 mg/ml in H<sub>2</sub>O), 20 μl of pepstatin (10 mg/ml in H<sub>2</sub>O), 200 μl of aprotinin (2 mg/ml in H<sub>2</sub>O), and 9.72 ml of water to a total 10 ml volume. Mix and freeze 500 μl aliquots at –80°C. For 100× phenylmethylsulfonyl fluoride (PMSF), dissolve 17.4 mg of PMSF in 1 ml of 100% ethanol (100 mM stock).

BMK-DKO, BMK-DKO<sup>C</sup>BCL-XL, BMK-DKO<sup>C</sup>BCL-2, BMK-DKO<sup>C</sup>BCL-W, and BMK-DKO<sup>C</sup>MCL-1 cells were grown to 80% confluency in a 10-cm dish. Cells were trypsinized, washed with phosphate-buffered saline (PBS), lysed in cold radioimmunoprecipitation assay buffer [150 mM NaCl, 1.0% Triton X-100, 0.5% sodium deoxycholate, 0.1% SDS, 50 mM tris (pH 8.0), and 1 mM EDTA and add fresh 1× PMSF and 2× PIN], incubated for 30 min on ice, and centrifuged at 13,000g and 4°C for 5 min. The supernatant was diluted to 2 mg/ml and diluted to 1 mg/ml in SDS–polyacrylamide gel electrophoresis loading buffer (reducing). Total protein (10 μg) was loaded per lane in immunoblots displayed in fig. S1A. In another experiment, BMK-DKO<sup>C</sup>MCL-1 cells were seeded (day 1) and treated with BH3 mimetic (listed above blot) or MG-132 (day 2) for 24 hours before cell lysis (as above) on day 3. Mouse GFP monoclonal antibody (mAb) was used to detect mCerulean3 fused to each antiapoptotic protein (1:2000 primary and 1:10,000 secondary; Peroxidase AffiniPure Donkey Anti-Mouse IgG). Blots were stripped for glyceraldehyde-3-phosphate dehydrogenase (GAPDH) rabbit mAb loading control (1:5000 primary and 1:10,000 secondary; Peroxidase AffiniPure Donkey Anti-Rabbit IgG).

### Fluorescence and absorbance spectra

Data in fig. S3C and fig. S6C were acquired on a Tecan Infinite M1000 microplate reader. Emission spectra were acquired for 5 μM mCerulean3 by excitation at 280 nm and emission from 400 to 850 nm. Absorbance spectra were acquired for 100 μM ABT-199 diluted in PBS (*n* = 1). Buffer alone was measured for each acquisition to subtract background, and all spectra were normalized to the maximum and plotted in GraphPad prism.

### INO-FHS microscope

Our qF<sup>3</sup> method and analysis can be implemented on other FLIM-FRET systems (28, 78–81) built for rapid FLIM-FRET screening applications. A detailed description of the INO-FHS microscope

build is included in the Supplementary Materials and illustrated in fig. S2. The INO-FHS is a multiplexed custom-built system for FLIM-FRET data acquisition. Time-correlated single photon counting (TCSPC) is performed in the donor channel; the incoming signal is split evenly into eight single-photon avalanche photodiode detectors, and as a result, we achieve rapid imaging speeds required for screening. System multiplexing allows the operation of the INO-FHS up to 40% TCSPC limit (82, 83). The acceptor emission is directed to the hyperspectral module, which consists of a spectral disperser and a  $2 \times 32$  channel photomultiplier tube. Unlike the FLIM module, the hyperspectral detection is not synchronized to the excitation source; thus, all incoming photons are detected during the acquisition period. This ensures that all photons are collected in the spectral channel. INO-FHS micrographs acquired for our qF<sup>3</sup> screen are 200  $\mu\text{m}$  by 200  $\mu\text{m}$  in size with 600  $\times$  600 pixel resolution.

### Standard curves for purified fluorescence proteins

Constructs used include His<sub>6</sub>-TEV-Venus-pBluescript and His<sub>6</sub>-TEV-mCerulean3-pBluescript. BL21-AI One Shot Chemically Competent *Escherichia coli* bacteria express Venus and mCerulean3 proteins with an N-terminal histidine tag upon induction with arabinose. mCerulean3 and Venus fluorophores were purified by nickel column chromatography (see Table 2 for the link). Since fluorescence of these proteins interfered with bicinchoninic acid, A280, and Bradford assays, the concentration of each fluorophore was determined by comparison to known concentrations of purified BCL-XL (~30 kDa; fig. S3A) (52). Expected excitation and emission peaks and average lifetime ( $\tau$ ) were confirmed for mCerulean3 (excitation, 433 nm; emission, 475 nm;  $\tau = 3.8$  ns) (64) and Venus (excitation, 515 nm; emission, 528 nm;  $\tau = 2.9$  ns; fig. S3, B and C) (84) from 5  $\mu\text{M}$  samples. Serial dilutions from 50 to 0.5  $\mu\text{M}$  fluorescence proteins (250- $\mu\text{l}$  aliquots) were stored at  $-80^\circ\text{C}$ . For each qF<sup>3</sup> experiment, standard concentrations of each fluorophore were imaged. To generate standard curves to determine the local mCerulean3 concentrations in cells, the standard solutions were analyzed for intensity per pixel at time 0 (T0) in the lifetime decay and plotted against concentration. For Venus, the intensity at wavelength 530 nm in the hyperspectral channel was plotted against Venus concentrations (fig. S3D).

From our purified fluorophore standards, we determined a known range of mCerulean3 (0 to 8  $\mu\text{M}$ ) and Venus (0 to 50  $\mu\text{M}$ ) for which the relationship between intensity and concentration was consistently linear (fig. S3D). In detail, the appropriate settings for 433-nm excitation for FLIM of mCerulean3 in live cells were determined to be ~5- $\mu\text{W}$  excitation laser power at the objective based on there being no photobleaching after 50 scans of the same field of view. To increase speed but hold the total photon dose roughly equivalent, the laser power was increased in small increments and the scan time was decreased so that the resulting counts per pixel remained approximately the same until we determined the TCSPC limit of the system. We then selected a laser power and scan time below this point as optimal for imaging. Laser power for the acceptor excitation was chosen such that the hyperspectral detector did not saturate operating at maximum sensitivity. With these settings, TCSPC saturation was observed for pixels with concentrations of mCerulean3 >10  $\mu\text{M}$ , and there was no saturation in the hyperspectral channel at 530 nm up to 43  $\mu\text{M}$ , the highest concentration of Venus. For each experiment, standard curves for purified

fluorescence proteins from 0.5 to 8  $\mu\text{M}$  mCerulean3 and 0.5 to 43  $\mu\text{M}$  Venus were measured. Saturation in binding for 2  $\mu\text{M}$  mCerulean3-fused antiapoptotic protein was achieved at ~10 to 20  $\mu\text{M}$  Venus-BH3 protein, which is typical for most biochemical binding experiments. Therefore, it was not necessary to extrapolate the linear correlation between intensity and concentration beyond the standard curves. We also considered  $K_d$  estimations beyond this range irrelevant, as there will be no relevant binding in live cells for apoptosis proteins with a  $K_d > 20$   $\mu\text{M}$ .

### Estimating concentrations in cells

Typically, obtaining sufficient photon counts for accurate measurement of FLIM requires binning of the data, markedly reducing spatial resolution. One qF<sup>3</sup> innovation enabling the acquisition of high-spatial resolution binding data is the binning of pixels within automatically selected subcellular regions of interest (ROIs) before lifetime analysis rather than analyzing individual pixels or using a fixed kernel (fig. S4A). Local concentrations of c<sub>antiapoptotic</sub> and v<sub>BH3</sub> proteins were measured by comparison of intensity per ROI to standard curves of purified mCerulean3 and Venus proteins (fig. S3, A to D) as previously (28), except without extrapolation. The advantages of qF<sup>3</sup> for determining concentrations in cells include the following: The intensity at T0 in the fluorescence lifetime decay is unaffected by FRET (28); Venus (acceptor) cross-talk is minimized by interleaved excitation and synchronized detection; and FRET-stimulated emission of the acceptor was corrected using the measured G factor of the instrument (fig. S3, E to G). Furthermore, phasor lifetime analysis (34) enables calculation of the fractional change in angular frequency  $\Delta\omega$ , a value directly related to the fraction of donor molecules in the bound versus unbound state, enabling determination of the concentration of unbound Venus ( $\text{Venus}_{\text{Free}}$ ).

In detail, from each fluorescence lifetime decay, we determined the average change in the lifetime and the total photons at the first part of the decay (T0). FRET occurs on a nanosecond time scale; thus, photons emitted immediately after the excitation pulse (picosecond time scale) come almost exclusively from donor molecules that have not undergone FRET (28). Thus, the number of photons emitted at T0 is proportional to the total number of donor molecules. This relationship is not well exploited in typical FLIM-FRET analysis because the limited number of photons collected at T0 in a single pixel is too small for accurate quantization. As a result, quantization errors confound measuring dynamic changes in fluorophore concentrations. Our ROI-based segmentation and binning approach (fig. S4A) mitigates quantization errors by combining photon counts from multiple pixels to ensure good counting statistics. Furthermore, the excitation of Venus contributes negligible counts in the FLIM channel (fig. S3E). Thus, intensity observed in cells at T0 can be directly compared to our mCerulean3 standard curve to convert to units of concentration without further correction.

The points on a phasor plot (e.g., fig. S4B) are generated by Fourier transformation of the lifetime decay data (34, 85). If the average position of sampled points falls on the perimeter of the plot in Fourier space (the universal semicircle), then the fluorescence decay of the sample can be fitted with a single component exponential. If not, then the sample is composed of donor molecules in more than one state, e.g., donor bound and unbound to an acceptor. Multicomponent lifetimes fall within the universal semicircle and

appear spread between the discrete lifetimes of the donor alone and the donor undergoing the theoretical maximum FRET (at distance 0) with the acceptor. Typically, the  $\tau_2$  position for any particular donor (the lifetime when all donors are undergoing maximal FRET with acceptors) is determined by extrapolating a straight line from  $\tau_1$  through the data for standards undergoing different amounts of FRET (fig. S3G) to  $\tau_2$ , the point of intersection on the universal semicircle. The  $\tau_2$  position in phasor space for the mCerulean3-Venus pair was determined from standard linker constructs (68, 86) with FRET efficiencies from 5 to 45% that collectively projected toward a single  $\tau_2$  position on the universal semicircle (fig. S3G). As expected, in live cells expressing mCerulean3-fused antiapoptotic proteins and the different <sup>V</sup>BH3 proteins, the resulting FRET data fit along the same line.

The fraction of bound donor molecules (bound fraction) can, in principle, be determined for any sample by measuring the  $\tau$  position between  $\tau_1$  at saturation ( $\tau_s$ ) along the line between  $\tau_1$  and  $\tau_2$  (fig. S4B) and by assuming that, at  $\tau_s$ , all of the donors are occupied by acceptor molecules. However, unlike  $\tau_2$ , which is a fixed value for any donor-acceptor pair, at saturation,  $\tau_s$  is determined by both the geometry (distance and dipole angle) between the donor and acceptor and  $\tau_2$  for the donor-acceptor pair. For these reasons,  $\tau_s$  varies for every <sup>V</sup>BH3 protein-C antiapoptotic protein pair. In addition, uncertainties in off-rate and competition from unknown concentrations of other competitors in cells make it difficult to determine whether all the donors are occupied by acceptor molecules at  $\tau_s$ . Furthermore, determining the point along the line that represents  $\tau_s$  has a large margin of error compared to the estimate of  $\tau_2$  obtained using standards. For these reasons, we measured the fractional change in angular frequency ( $\Delta\omega$ ), which is the fractional distance along the line from  $\tau_1$  to  $\tau_2$  instead of estimating bound fraction. Because  $\Delta\omega$  can be determined accurately and it is directly related to bound fraction, the  $\Delta\omega$  values can be fit to a Hill equation to determine an apparent  $K_d$  that is a more accurate estimate of binding than can be obtained by other methods. Determining  $K_d$  values requires substantial data analysis, which rapidly becomes a bottleneck for screening. Therefore, unlike other systems that fit the data for every pixel, we select ROIs and bin the data before determining  $\Delta\omega$  for a two-component model using the phasor approach (fig. S4, A and B). This improves temporal measurement by increasing the signal, reducing noise, and markedly reducing computation time.

We accounted for the increase in acceptor intensity observed in the hyperspectral channel due to FRET by measuring the instrument  $G$  factor (see Table 2 for a link to the step-by-step protocol). In a manner resembling a three-cube FRET experiment (87), we imaged BMK-DKO cells expressing mCerulean3-Venus joined with linkers of different lengths (fig. S3G) with three different excitation configurations: #1, acceptor (510 nm) excitation only; #2, donor + acceptor (510 nm + 433 nm) excitation; and #3, donor excitation (433 nm) only. As is common practice for determining  $G$  factor (87), we assume a 1:1 mCerulean3:Venus ratio for constructs in which the two proteins are expressed as fusion proteins with linker peptides of different lengths. After bleed-through subtraction (fig. S3F) and conversion of the hyperspectral intensity to concentration (fig. S3D), we observed an apparent concentration of Venus ( $Venus_{\text{Apparent}}$ ) that was greater than the known  $Venus_{\text{Total}}$

$$Venus_{\text{Apparent}} = Venus_{\text{Total}} + Venus_{\text{Overestimated}} \quad (2)$$

where  $Venus_{\text{Overestimated}}$  is the overestimated concentration in Venus due to sensitized emission.

$Venus_{\text{Apparent}}$  was determined by comparing the hyperspectral intensity at 530 nm per ROI to the Venus protein standard curve. Data from two biological replicates were combined, plotted in three dimensions (fig. S3G), and then fit to determine the  $G$  factor of our instrument (7.93) using the equation

$$E f_{\text{bound}} = \frac{Venus_{\text{Overestimated}}/G}{\gamma(mCerulean3_{\text{Total}} + Venus_{\text{Overestimated}}/G)} \quad (3)$$

where “ $E$ ” is the FRET efficiency (determined by lifetime analysis), “ $f_{\text{bound}}$ ” is the fraction of bound donor, “ $G$ ” is the  $G$  factor, and “ $\gamma$ ” is a scaling parameter. For the tethered fluorophore dimers,  $f_{\text{bound}}$  is assumed to be 1. This equation can be rearranged as

$$Venus_{\text{Overestimated}} = \frac{G(mCerulean3_{\text{Total}}E)}{\gamma + E} \quad (4)$$

In this way, the  $G$  factor was used to correct hyperspectral measurements for Venus concentration by subtracting  $Venus_{\text{Overestimated}}$ .

### Capturing a range of acceptor:donor levels for FLIM-FRET binding curves

As reviewed earlier, we use phasor plots as a rapid accurate method to measure FRET. By making FRET measurements in which the donor concentration is relatively constant and the acceptor concentration is varied from zero to a concentration in which binding has saturated, it is possible to fit the data to a Hill equation and determine a binding constant. To do this, we use cells in which the donor is stably expressed and the acceptor is expressed by transient transfection. Thousands of ROIs are selected, and the lifetime measurements from these ROIs with widely varying ratios of donor and acceptor are determined. Together with concentration measurements, these data can be fit to a binding curve. Protein-protein interactions result in FRET that increases in a hyperbolic manner with acceptor concentration until it reaches a plateau when all available donor molecules have interacted with an acceptor.

The photon counting rate of the donor fluorophore at T0 estimates the intensity of the donor because, at short times, energy transfer, which decreases donor intensity, has not occurred. Using the instrument  $G$  factor and a hyperspectral detector, the intensity of the acceptor is determined. Intensities are converted to concentrations using standard curves generated from measurements of purified proteins recorded in the same experiment. The FRET and concentration data are fit with a Hill equation to determine binding constants. The frequency of random collisions increases markedly when two proteins are localized to the same compartment or membrane surface. In this situation, random collisions can generate FRET signals comparable to that of a true protein-protein interaction. However, FRET due to collisions increases linearly with concentration. Although this means that binding can be distinguished from collisions by the shape of the curve, the best practice is to define “binding versus nonbinding” for two proteins by including a nonbinding mutant with similar subcellular localization to the positive control (referred to as the collisional or negative control).

### BH3 mimetic stocks

BH3 mimetics were dissolved in fresh anhydrous DMSO to make 20 mM stocks, and 5- $\mu$ l aliquots were stored at  $-80^{\circ}\text{C}$ , desiccated. Stocks were never thawed more than twice. To achieve a consistent amount of DMSO per well in the screen, 1000 $\times$  stocks for the serial dilutions were made in DMSO.

### Preparing 384-well plate for qF<sup>3</sup> screen

See Table 2 for a link to Protocol Exchange, where we provide step-by-step instructions for preparing a sample plate of cells including a checklist of controls to include in each screen. Note that a biological replicate refers to a plate of cells seeded, transfected, treated, and imaged separately. Briefly, BMK-DKO cells stably expressing a mCerulean3 fusion antiapoptotic protein were seeded at 3000 cells per well into a CellCarrier-384 Ultra microplate. After 24 hours, wells were transfected with plasmids encoding <sup>V</sup>BH3 proteins or <sup>V</sup>BH3-4E collisional control proteins, using TransIT-X2 reagent (Mirus). pSPUTK DNA was added to transfection reactions to maintain the required amount of DNA for efficient transfection while controlling the overexpression of the protein of interest. “Untransfected” wells were treated with transfection reagent alone (no DNA added). Medium was changed after 3 to 5 hours. At this time, selected wells were treated with BH3 mimetic. BH3 mimetic stocks and DMSO (solvent control) were diluted 1000 $\times$  in DMEM complete media before adding to wells. Sample plates were incubated for 12 to 18 hours, and without changing the media, image data were collected for the live cells. Immediately before imaging, fluorescence protein standards were added to empty wells. Fluorescein (10 nM in 0.1 M NaOH) and quenched fluorescein [30  $\mu$ M fluorescein in 8.3 M NaI and 100 mM Na<sub>2</sub>HPO<sub>4</sub> (pH 10)] were also added to the plate for instrument calibration.

### Data acquisition for qF<sup>3</sup> screen

A step-by-step protocol for the operation of the INO-FHS microscope was published (83) and summarized in our associated Protocol Exchange submission (see Table 2 for the link). The sample plate is incubated at 25 $^{\circ}\text{C}$  and 5% CO<sub>2</sub> for the duration of the experiment (completed within 24 hours). Using the same settings to be used for collecting images of cells, we acquire at least two images for each concentration of purified mCerulean3 and Venus to construct fluorescence intensity versus concentration standard curves. The automated acquisition is managed using Nikon Elements software that communicates with the INO-FHS acquisition software via a custom macro. We specify that each subsequent field of view be acquired only after the entire 384-well plate is scanned, thereby minimizing the time between wells. Four images were sufficient for samples with good transfection efficiency and high FRET efficiency; however, up to 10 images were required for more difficult samples, i.e., <sup>C</sup>MCL-1 protein-protein interactions.

### Fast semisupervised qF<sup>3</sup> analysis

A step-by-step analysis procedure is described in our associated Protocol Exchange submission (see Table 2 for the link). In summary, each replicate was analyzed to generate binned binding curves for each well in the screen (fig. S4B); then, three or more biological replicates were combined and fit to a Hill equation to generate the final binding curves (fig. S4C). The apparent binding constants derived from these data are displayed as heatmaps. The ROI data were binned by Venus<sub>free</sub> concentration to facilitate normalization

(fig. S4B) before combining the data from 3+ biological replicates (fig. S4C).

The analysis is split into steps, allowing users to examine data, troubleshoot, and input desired changes at each stage in the pipeline. For step 1, we compress data to reduce file size up to  $1/16$  of the original size; for step 2, we analyze the purified fluorescent proteins and establish standard curves. For step 3, we process “INO.TIFF” data to select ROI data. For step 4, we combine all data for individual wells in the 384-well plate. For step 5, we convert intensity to concentration, determine  $\Delta\omega$  per ROI, and filter resulting data to extract binding curves. For step 6, we convert phasor coordinates to average lifetime per well for untransfected controls and assess whether treatment makes a substantial impact on mCerulean3 lifetime (greater than 0.1 ns), because of energy transfer from the fluorescent protein to the inhibitor molecule. For step 7, we extract data for analysis on the basis of concentrations (1 to 3  $\mu$ M mCerulean3 and 0 to 50  $\mu$ M Venus) and then bin ROI data by free Venus concentration to extract binned binding curves. Steps 1 to 7 are repeated for three biological replicates of a screen.

From images collected on the INO-FHS, ROIs are automatically identified via a watershed algorithm applied to the TCSPC channel. Pixels within each ROI were binned, reducing the contribution of background pixels to the calculated lifetimes and reducing the number of decay curves to fit per image. As mentioned earlier, we measure  $\Delta\omega$  from the phasor analysis as a surrogate for a bound fraction for fitting the data to a Hill equation. The  $\Delta\omega$  for each ROI is determined by measuring the normalized distance of  $\tau$  along the dashed line from the average position of  $\tau_1$  to  $\tau_2$  (fig. S4B).

The concentration of mCerulean3 and Venus per ROI is measured, and assuming 1:1 binding, we calculate free Venus (Venus<sub>free</sub>). The final qF<sup>3</sup> binding curves may be examined in three dimensions (e.g., fig. S4B for <sup>C</sup>BCL-W binding to <sup>V</sup>BIML). Higher levels of <sup>C</sup>BCL-W were observed in BMK-DKO cells compared to our other cell lines (fig. S3H). Notably, the live-cell  $K_d$  depended on the concentration of donor present (fig. S3I). Thus, we selected a narrow physiologically relevant (36) range of mCerulean3 expression (1 to 3  $\mu$ M) for our two-dimensional binding curves, applied before binning ROI data by the concentration of Venus<sub>free</sub>. Binning equalizes the number of points per curve before combining biological replicates.

In analysis step 8, data from three or more replicates are combined to generate our final binding curves; then, in step 9, final binding curves are analyzed as shown in fig. S4C. For positive (<sup>V</sup>BH3) and negative (<sup>V</sup>BH3-4E) controls treated with DMSO, we determine the median  $\Delta\omega$  for points that fall within 10 to 20  $\mu$ M Venus<sub>free</sub>. The difference in median  $\Delta\omega$  for these control curves ( $\Delta\beta$ ) was used as a criterion for screening: We consider detected binding insufficient for screening if  $\Delta\beta$  was less than 0.05 (e.g., see fig. S5A). If sufficient binding was detected, we calculated %drug resistance for all treated wells as previously described (26). Furthermore, we calculated sRatio, a value that is independent of maximum bound fraction and can be calculated without fitting (see Materials and Methods). On the basis of simulated and experimental data, we set a minimum sRatio threshold of 2 (fig. S5, B and C) to proceed with the fitting analysis. For each curve, the “saturation parameter” (B<sub>max</sub>) was estimated from the median of the points in the far right of each binding curve (30 to 50  $\mu$ M Venus<sub>free</sub>). These fitting parameters determined from positive control wells were then applied to fit corresponding <sup>V</sup>BH3-4E mutant and <sup>V</sup>BH3-treated wells. From each curve, we export the number of points analyzed, number of



binned points in the final binding curve, cumulative sum of the area under the curve, median  $\Delta\omega$  at 10 to 20  $\mu\text{M}$  Venus<sub>Free</sub>, %resistance to displacement by treatment, and  $K_d$  with upper and lower confidence interval ( $\mu\text{M}$ ). In step 10, we plot each individual curve along with the fit for users to view any binding curve analyzed. In step 11, we run a script that calculates the average donor concentration per well. Step 12 converts total results into a 384-well plate format for generating heatmaps. Last, in step 13, we combine all untransfected lifetime data for our controls to generate data in fig. S6 (A and B).

When combining data from multiple screens ( $n > 3$  for each screen), we displayed the average  $K_d$  from all screens, combined. In each heatmap, “binding” was represented in blue and “no binding” was represented in red. However, the colors are strictly for visualization, and the corresponding numbers are also provided in each cell of the heatmaps.

### Quality control: sRatio

If a sample contains mostly collisions or substantial noise and a low FRET signal, then the data do not reach saturation within the range of the expressed proteins and, therefore, cannot be usefully fit to a Hill equation for binding. To identify these samples automatically, we calculate an sRatio for the binding data. To calculate the sRatio, the data are sorted by Venus<sub>Free</sub> and the boundaries for the area of the plot are determined for each curve. The lower boundary is set at fractional change = 0 and the concentration of Venus<sub>Free</sub> = 0  $\mu\text{M}$ . The upper boundary is determined as the median fractional change/concentration Venus<sub>Free</sub> of the last six points on the binding curve. If the upper boundary is not greater than our minimum  $\Delta\beta$  (0.05), then the upper boundary is set to 0.05. In addition, to ensure that the sRatio is always a positive value, points above/below the upper and lower boundaries are removed. Then, we determine the isotonic fit of the data (fig. S4C, red line in the middle graph) and find the areas above and below the isotonic fit within the boundaries of the plot. The simulated binding curves for a range of  $K_d$ 's highlight the relationship between  $K_d$  and sRatio (fig. S5B). If Bmax is reached at a concentration of Venus<sub>Free</sub> > 50  $\mu\text{M}$ , then Bmax is outside the range that we sample with our binding curves. Furthermore,  $K_d$  values greater than approximately 20  $\mu\text{M}$  suggest that there is no binding in live cells. We, therefore, selected an sRatio threshold of 2 (corresponding to  $K_d \sim 25 \mu\text{M}$ ) as the minimum required for fitting the data to a Hill equation. Consistent with expectation, we observed that most of our <sup>V</sup>BH3-4E collisional controls do not pass this threshold, whereas known protein-protein interactions did (fig. S5C).

### Quality control: Drug effect on donor lifetime

To avoid false positives or false negatives due to incorrect fluorescence lifetime fitting, we include a quality control step, where the user examines whether each compound has a marked effect on donor lifetime (fig. S6). Such compounds must be dropped from a qF<sup>3</sup> screen. For example, here, we found that ABT-199 acts as a FRET acceptor for mCerulean3. The efficacy of BCL-2 inhibitor ABT-199 has been demonstrated in multiple cell lines and the clinic (9). Hence, we expected a high efficacy of this compound for inhibiting BH3 protein binding to BCL-2. However, in a concentration-dependent manner, ABT-199 affects the lifetime of the mCerulean3 donor bound to BCL-2, BCL-XL, and BCL-W but not MCL-1 (fig. S6, A and B), complicating the data analysis and suggesting that ABT-199 functions as an acceptor for FRET with mCerulean3. The fluorescence decays measured by qF<sup>3</sup> for potential competition

between ABT-199 and BH3 protein binding to antiapoptotic protein result in at least three components, which meant that the data were too complicated to analyze reliably. As a result, ABT-199 failed criteria for screening by qF<sup>3</sup> for BCL-2, BCL-XL, and BCL-W. Using this change in the fluorescence lifetime as a readout for binding of ABT-199 to antiapoptotic proteins in cells, we demonstrate a higher binding affinity for BCL-2 than BCL-XL, low affinity for BCL-W, and no affinity for MCL-1 (fig. S6, A and B). The resulting  $K_d$  values suggest that ABT-199 binds to BCL-2 at least three orders of magnitude better than BCL-XL and more than six orders of magnitude better than BCL-W (fig. S6). Thus, for fluorescent drugs or fluorescent analogs, change in mCerulean3 lifetime can be used to measure binding directly, but we cannot extend these data to demonstrate binding to the BH3 binding groove or inhibition of BH3 protein binding.

### Calculating %resistance

As previously described (26) and illustrated in Fig. 4E, we also calculate the %resistance calculation to drug displacement as a measure of drug efficacy. Points between 10 and 20  $\mu\text{M}$  free Venus are binned, and the median fractional change is determined for the protein of interest (A), the corresponding collisional control (B), and protein of interest + drug (C). The 10 to 20  $\mu\text{M}$  range was selected for our analysis on the basis of the observed point of inflection for most binding curves analyzed here. The user has the option to change/extend this range if their point of inflection is different. The difference in median  $\Delta\omega$  between the protein of interest and collisional control “ $\Delta\beta$ ,” described earlier, while the difference in  $\Delta\omega$  between the protein of interest + drug and the collisional control is  $C - B$  (Fig. 4E). Thus, if  $(C - B) \geq \Delta\beta$ , then the drug is ineffective and %resistance is 100%. On the other hand, if  $(C - B) < \Delta\beta$ , then the drug reduced binding.

%Resistance only captures information within a small window of the binding curve in comparison to  $K_d$ , which fits all data. When the dynamic range, i.e.,  $\Delta\beta$ , is small, the variations in the replicates rapidly limit measurement certainty. Here, consistent with the measurement of  $K_d$ , we consider  $\Delta\beta > 0.05$  as required to calculate %resistance. This was not previously defined in our previous publication (26), and this automates the decision to examine %resistance data for each protein-protein interaction in the screen.

### SUPPLEMENTARY MATERIALS

Supplementary material for this article is available at <https://science.org/doi/10.1126/sciadv.abm7375>

[View/request a protocol for this paper from Bio-protocol.](#)

### REFERENCES AND NOTES

1. C. Akgul, D. A. Moulding, M. R. White, S. W. Edwards, In vivo localisation and stability of human Mcl-1 using green fluorescent protein (GFP) fusion proteins. *FEBS Lett.* **478**, 72–76 (2000).
2. L. P. Billen, A. Shamas-Din, D. W. Andrews, Bid: A Bax-like BH3 protein. *Oncogene* **27**, S93–S104 (2008).
3. J. Lindsay, M. D. Esposti, A. P. Gilmore, Bcl-2 proteins and mitochondria-specificity in membrane targeting for death. *Biochim. Biophys. Acta, Mol. Cell Res.* **1813**, 532–539 (2011).
4. J. C. Gómez-Fernández, Functions of the C-terminal domains of apoptosis-related proteins of the Bcl-2 family. *Chem. Phys. Lipids* **183**, 77–90 (2014).
5. X. Chi, D. Nguyen, J. M. Pemberton, E. J. Osterlund, Q. Liu, H. Brahmbhatt, Z. Zhang, J. Lin, B. Leber, D. W. Andrews, The carboxyl-terminal sequence of bim enables bax activation and killing of unprimed cells. *eLife* **9**, e44525 (2020).
6. S. Banjara, C. D. Suraweera, M. G. Hinds, M. Kvensakul, The Bcl-2 family: Ancient origins, conserved structures, and divergent mechanisms. *Biomolecules* **10**, 128 (2020).



7. E. F. Lee, W. D. Fairlie, The structural biology of Bcl-xL. *Int. J. Mol. Sci.* **20**, 2234 (2019).
8. M. Gentile, A. Petrungraro, G. Uccello, E. Vigna, A. G. Recchia, N. Caruso, S. Bossio, L. De Stefano, A. Palumbo, F. Storino, M. Martino, F. Morabito, Venetoclax for the treatment of chronic lymphocytic leukemia. *Expert Opin. Investig. Drugs* **26**, 1307–1316 (2017).
9. L. M. Juárez-Salcedo, V. Desai, S. Dalia, Venetoclax: Evidence to date and clinical potential. *Drugs Context* **8**, 212574 (2019).
10. C. Tse, A. R. Shoemaker, J. Adickes, M. G. Anderson, J. Chen, S. Jin, E. F. Johnson, K. C. Marsh, M. J. Mitten, P. Nimmer, L. Roberts, S. K. Tahir, Y. Xiao, X. Yang, H. Zhang, S. Fesik, S. H. Rosenberg, S. W. Elmore, ABT-263: A potent and orally bioavailable Bcl-2 family inhibitor. *Cancer Res.* **68**, 3421–3428 (2008).
11. W. H. Wilson, O. A. O'Connor, M. S. Czuczman, A. S. LaCasce, J. F. Gerecitano, J. P. Leonard, A. Tulpule, K. A. Dunleavy, H. Xiong, Y.-L. Chiu, Y. Cui, T. Busman, S. W. Elmore, S. H. Rosenberg, A. P. Krivoshik, S. H. Enschede, R. A. Humerickhouse, Navitoclax, a targeted high-affinity inhibitor of BCL-2, in lymphoid malignancies: A phase 1 dose-escalation study of safety, pharmacokinetics, pharmacodynamics, and antitumor activity. *Lancet Oncol.* **11**, 1149–1159 (2010).
12. C. M. Rudin, C. L. Hann, E. B. Garon, M. R. de Oliveira, P. D. Bonomi, D. R. Camidge, Q. Chu, G. Giaccone, D. Khaira, S. S. Ramalingam, M. R. Ranson, C. Dive, E. M. McKeegan, B. J. Chyla, B. L. Dowell, A. Chakravarty, C. E. Nolan, N. Rudersdorf, T. A. Busman, M. H. Mabry, A. P. Krivoshik, R. A. Humerickhouse, G. I. Shapiro, L. Gandhi, Phase II study of single-agent navitoclax (ABT-263) and biomarker correlates in patients with relapsed small cell lung cancer. *Clin. Cancer Res.* **18**, 3163–3169 (2012).
13. S.-P. Tzung, K. M. Kim, G. Basañez, C. D. Giedt, J. Simon, J. Zimmerberg, K. Y. Zhang, D. M. Hockenbery, Antimycin A mimics a cell-death-inducing Bcl-2 homology domain 3. *Nat. Cell Biol.* **3**, 183–191 (2001).
14. L. Wang, G. A. Doherty, A. S. Judd, Z.-F. Tao, T. M. Hansen, R. R. Frey, X. Song, M. Bruncko, A. R. Kunzer, X. Wang, M. D. Wendt, J. A. Flygare, N. D. Catron, R. A. Judge, C. H. Park, S. Shekhar, D. C. Phillips, P. Nimmer, M. L. Smith, S. K. Tahir, Y. Xiao, J. Xue, H. Zhang, P. N. Le, M. J. Mitten, E. R. Boghaert, W. Gao, P. Kovar, E. F. Choo, D. Diaz, W. J. Fairbrother, S. W. Elmore, D. Sampath, J. D. Levenson, A. J. Souers, Discovery of A-1331852, a first-in-class, potent, and orally-bioavailable BCL-XL inhibitor. *ACS Med. Chem. Lett.* **11**, 1829–1836 (2020).
15. H. Zhou, J. Chen, J. L. Meagher, C.-Y. Yang, A. Aguilar, L. Liu, L. Bai, X. Cong, Q. Cai, X. Fang, J. A. Stuckey, S. Wang, Design of Bcl-2 and Bcl-xL inhibitors with subnanomolar binding affinities based upon a new scaffold. *J. Med. Chem.* **55**, 4664–4682 (2012).
16. D. Park, A. T. Magis, R. Li, T. K. Owonikoko, G. L. Sica, S.-Y. Sun, S. S. Ramalingam, F. R. Khuri, W. J. Curran, X. Deng, Novel small-molecule inhibitors of Bcl-XL to treat lung cancer. *Cancer Res.* **73**, 5485–5496 (2013).
17. P. Casara, J. Davidson, A. Claperon, G. L. Le Toumelin-Braizat, M. Vogler, A. Bruno, M. Chanrion, G. Lysiak-Auvity, T. Le Diguarher, J. B. Starck, I. Chen, N. Whitehead, C. Graham, N. Matassova, P. Dokurno, C. Pedder, Y. Wang, S. Qiu, A. M. Girard, E. Schneider, F. Gravé, A. Studeny, G. Guasconi, F. Rocchetti, S. Maiga, J. M. Henlin, F. Colland, L. Kraus-Berthier, S. L. Le Gouill, M. J. S. Dyer, R. Hubbard, M. Wood, M. Amiot, G. M. Cohen, J. A. Hickman, E. Morris, J. Murray, O. Geneste, S55746 is a novel orally active BCL-2 selective and potent inhibitor that impairs hematological tumor growth. *Oncotarget* **9**, 20075–20088 (2018).
18. S. Fletcher, MCL-1 inhibitors—Where are we now (2019)? *Expert Opin. Ther. Pat.* **29**, 909–919 (2019).
19. S. B. Balachander, S. W. Criscione, K. F. Byth, J. Cidado, A. Adam, P. Lewis, T. Macintyre, S. Wen, D. Lawson, K. Burke, T. Lubinski, J. W. Tyner, S. E. Kurtz, S. K. McWeeney, J. Varnes, R. B. Diebold, T. Gero, S. Ioannidis, E. J. Hennessy, W. McCoull, J. C. Saeh, A. Tabatabai, O. Tavana, N. Su, A. Schuller, M. J. Garnett, P. Jaaks, E. A. Coker, G. P. Gregory, A. Newbold, R. W. Johnstone, E. Gangl, M. Wild, M. Zinda, J. P. Secrist, B. R. Davies, S. E. Fawell, F. D. Gibbons, AZD4320, a dual inhibitor of Bcl-2 and Bcl-xL, induces tumor regression in hematologic cancer models without dose-limiting thrombocytopenia. *Clin. Cancer Res.* **26**, 6535–6549 (2020).
20. G. Wang, Z. Nikolovska-Coleska, C. Y. Yang, R. Wang, G. Tang, J. Guo, S. Shangary, S. Qiu, W. Gao, D. Yang, J. Meagher, J. Stuckey, K. Krajewski, S. Jiang, P. P. Roller, H. O. Aboan, Y. Tomita, S. Wang, Structure-based design of potent small-molecule inhibitors of anti-apoptotic Bcl-2 proteins. *J. Med. Chem.* **49**, 6139–6142 (2006).
21. R. M. Sears, D. G. May, K. J. Roux, in *Methods in Molecular Biology* (Humana Press Inc., 2019), vol. 2012, pp. 299–313.
22. A. S. Shavkunov, S. R. Ali, N. I. Panova-Elektronova, F. Laezza, in *Methods in Molecular Biology* (Humana Press Inc., 2015), vol. 1278, pp. 497–514.
23. T. Machleidt, C. C. Woodroffe, M. K. Schwinn, J. Méndez, M. B. Robers, K. Zimmerman, P. Otto, D. L. Daniels, T. A. Kirkland, K. V. Wood, NanoBRET-A novel BRET platform for the analysis of protein-protein interactions. *ACS Chem. Biol.* **10**, 1797–1804 (2015).
24. W. R. Algar, N. Hildebrandt, S. S. Vogel, I. L. Medintz, FRET as a biomolecular research tool—Understanding its potential while avoiding pitfalls. *Nat. Methods* **16**, 815–829 (2019).
25. A. Aranovich, Q. Liu, T. Collins, F. Geng, S. Dixit, B. Leber, D. W. Andrews, Differences in the mechanisms of proapoptotic BH3 proteins binding to Bcl-XL and Bcl-2 quantified in live MCF-7 cells. *Mol. Cell* **45**, 754–763 (2012).
26. Q. Liu, E. J. Osterlund, X. Chi, J. Pogmore, B. Leber, D. W. Andrews, Bim escapes displacement by BH3-mimetic anti-cancer drugs by double-bolt locking both Bcl-XL and Bcl-2. *eLife* **8**, e37689 (2019).
27. J. Pécot, L. Maillet, J. Le Pen, C. Vuillier, S. de Carné Trécesson, A. Fétiveau, K. A. Sarosiek, F. J. Bock, F. Braun, A. Letai, S. W. G. Tait, F. Gautier, P. P. Juin, Tight sequestration of BH3 proteins by BCL-xL at subcellular membranes contributes to apoptotic resistance. *Cell Rep.* **17**, 3347–3358 (2016).
28. A. Margineanu, J. J. Chan, D. J. Kelly, S. C. Warren, D. Flatters, S. Kumar, M. Katan, C. W. Dunsby, P. M. W. French, Screening for protein-protein interactions using Förster resonance energy transfer (FRET) and fluorescence lifetime imaging microscopy (FLIM). *Sci. Rep.* **6**, 28186 (2016).
29. Q. Liu, B. Leber, D. W. Andrews, Interactions of pro-apoptotic BH3 proteins with anti-apoptotic Bcl-2 family proteins measured in live MCF-7 cells using FLIM FRET. *Cell Cycle* **11**, 3536–3542 (2012).
30. M. Villalobos-Ortiz, J. Ryan, T. N. Mashaka, J. T. Opferman, A. Letai, BH3 profiling discriminates on-target small molecule BH3 mimetics from putative mimetics. *Cell Death Differ.* **27**, 999–1007 (2020).
31. A. J. Souers, J. D. Levenson, E. R. Boghaert, S. L. Ackler, N. D. Catron, J. Chen, B. D. Dayton, H. Ding, S. H. Enschede, W. J. Fairbrother, D. C. S. Huang, S. G. Hymowitz, S. Jin, S. L. Khaw, P. J. Kovar, L. T. Lam, J. Lee, H. L. Maecker, K. C. Marsh, K. D. Mason, M. J. Mitten, P. M. Nimmer, A. Aleksijew, C. H. Park, C.-M. Park, D. C. Phillips, A. W. Roberts, D. Sampath, J. F. Seymour, M. L. Smith, G. M. Sullivan, S. K. Tahir, C. Tse, M. D. Wendt, Y. Xiao, J. C. Xue, H. Zhang, R. A. Humerickhouse, S. H. Rosenberg, S. W. Elmore, ABT-199, a potent and selective BCL-2 inhibitor, achieves antitumor activity while sparing platelets. *Nat. Med.* **19**, 202–208 (2013).
32. H. Liu, M. J. Michmerhuizen, Y. Lao, K. Wan, A. H. Salem, J. Sawicki, M. Serby, S. Vaidyanathan, S. L. Wong, S. Agarwal, M. Dunbar, J. Sydor, S. M. de Moraes, A. J. Lee, Metabolism and disposition of a novel B-cell lymphoma-2 inhibitor venetoclax in humans and characterization of its unusual metabolites. *Drug Metab. Dispos.* **45**, 294–305 (2017).
33. U. S. F. and D. A. Abbvie Inc, Highlights of prescribing information, *Venclexta [package Inser. Approv. by U.S. Food Drug Adm. Revis. 10/2020]*, (2020), pp. 1–53.
34. S. Ranjit, L. Malacrida, D. M. Jameson, E. Gratton, Fit-free analysis of fluorescence lifetime imaging data using the phasor approach. *Nat. Protoc.* **13**, 1979–2004 (2018).
35. I. Jarmoskaite, I. AlSadhan, P. P. Vaidyanathan, D. Herschlag, How to measure and evaluate binding affinities. *eLife* **9**, e57264 (2020).
36. A. U. Lindner, C. G. Concannon, G. J. Boukes, M. D. Cannon, F. Llambi, D. Ryan, K. Boland, J. Kehoe, D. A. McNamara, F. Murray, E. W. Kay, S. Hector, D. R. Green, H. J. Huber, J. H. M. Prehn, Systems analysis of BCL2 protein family interactions establishes a model to predict responses to chemotherapy. *Cancer Res.* **73**, 519–528 (2013).
37. J. Kale, E. J. Osterlund, D. W. Andrews, BCL-2 family proteins: Changing partners in the dance towards death. *Cell Death Differ.* **25**, 65–80 (2018).
38. J. Áden, A. U. Mushtaq, A. Dingeldein, M. Wallgren, G. Gröbner, A novel recombinant expression and purification approach for the full-length anti-apoptotic membrane protein Bcl-2. *Protein Expr. Purif.* **172**, 105628 (2020).
39. M. Nguyen, D. G. Millar, V. W. Yong, S. J. Korsmeyer, G. C. Shore, Targeting of Bcl-2 to the mitochondrial outer membrane by a COOH-terminal signal anchor sequence. *J. Biol. Chem.* **268**, 25265–25268 (1993).
40. F. Janiak, B. Leber, D. W. Andrews, Assembly of Bcl-2 into microsomal and outer mitochondrial membranes. *J. Biol. Chem.* **269**, 9842–9849 (1994).
41. P. J. Dlugosz, L. P. Billen, M. G. Annis, W. Zhu, Z. Zhang, J. Lin, B. Leber, D. W. Andrews, Bcl-2 changes conformation to inhibit Bax oligomerization. *EMBO J.* **25**, 2287–2296 (2006).
42. Y. Te Hsu, R. J. Youle, Nonionic detergents induce dimerization among members of the Bcl-2 family. *J. Biol. Chem.* **272**, 13829–13834 (1997).
43. B. Leber, J. Lin, D. W. Andrews, Still embedded together binding to membranes regulates Bcl-2 protein interactions. *Oncogene* **29**, 5221–5230 (2010).
44. A. J. Smith, H. Dai, C. Correia, R. Takahashi, S. H. Lee, I. Schmitz, S. H. Kaufmann, Noxa/Bcl-2 protein interactions contribute to bortezomib resistance in human lymphoid cells. *J. Biol. Chem.* **286**, 17682–17692 (2011).
45. L. Bai, J. Chen, D. McEachern, L. Liu, H. Zhou, A. Aguilar, S. Wang, BM-1197: A novel and specific Bcl-2/Bcl-xL inhibitor inducing complete and long-lasting tumor regression in vivo. *PLOS ONE* **9**, e99404 (2014).
46. P. Gomez-Bougie, S. Maiga, B. Tessoulin, J. Bourcier, A. Bonnet, M. S. Rodriguez, S. Le Gouill, C. Touzeau, P. Moreau, C. Pellat-Deceunynck, M. Amiot, BH3-mimetic toolkit guides the respective use of BCL2 and MCL1 BH3-mimetics in myeloma treatment. *Blood* **132**, 2656–2669 (2018).
47. M. Certo, V. Del Gaudio Moore, M. Nishino, G. Wei, S. Korsmeyer, S. A. Armstrong, A. Letai, Mitochondria primed by death signals determine cellular addiction to antiapoptotic BCL-2 family members. *Cancer Cell* **9**, 351–365 (2006).
48. W. Nakajima, M. A. Hicks, N. Tanaka, G. W. Krystal, H. Harada, Noxa determines localization and stability of MCL-1 and consequently ABT-737 sensitivity in small cell lung cancer. *Cell Death Dis.* **5**, e1052 (2014).

49. S. Oppermann, J. Ylanko, Y. Shi, S. Hariharan, C. C. Oakes, P. M. Brauer, J. C. Zúñiga-Pflücker, B. Leber, D. E. Spaner, D. W. Andrews, High-content screening identifies kinase inhibitors that overcome venetoclax resistance in activated CLL cells. *Blood* **128**, 934–947 (2016).
50. B. M. Polster, G. Basañez, M. Young, M. Suzuki, G. Fiskum, Inhibition of Bax-induced cytochrome c release from neural cell and brain mitochondria by dibucaine and propranolol. *J. Neurosci.* **23**, 2735–2743 (2003).
51. C. Bogner, J. Kale, J. Pogmore, X. Chi, A. Shamas-Din, C. Fradin, B. Leber, D. W. Andrews, Allosteric regulation of BH3 proteins in Bcl-xL complexes enables switch-like activation of bax. *Mol. Cell* **77**, 901–912.e9 (2020).
52. L. P. Billen, C. L. Kokoski, J. F. Lovell, B. Leber, D. W. Andrews, Bcl-XL inhibits membrane permeabilization by competing with bax. *PLoS Biol.* **6**, e147 (2008).
53. R. S. Soderquist, A. Eastman, BCL2 inhibitors as anticancer drugs: A plethora of misleading BH3 mimetics. *Mol. Cancer Ther.* **15**, 2011–2017 (2016).
54. M. G. Hinds, M. Lackmann, G. L. Skea, P. J. Harrison, D. C. S. Huang, C. L. Day, The structure of Bcl-W reveals a role for the C-terminal residues in modulating biological activity. *EMBO J.* **22**, 1497–1507 (2003).
55. Y. Yao, L. M. Fujimoto, N. Hirshman, A. A. Bobkov, A. Antignani, R. J. Youle, F. M. Marassi, Conformation of BCL-XL upon membrane-integration. *J. Mol. Biol.* **427**, 2262–2270 (2015).
56. J. M. Pemberton, J. P. Pogmore, D. W. Andrews, Neuronal cell life, death, and axonal degeneration as regulated by the BCL-2 family proteins. *Cell Death Differ.* **28**, 108–122 (2021).
57. K. D. Mason, M. R. Carpinelli, J. I. Fletcher, J. E. Collinge, A. A. Hilton, S. Ellis, P. N. Kelly, P. G. Ekert, D. Metcalf, A. W. Roberts, D. C. S. Huang, B. T. Kile, Programmed anuclear cell death delimits platelet life span. *Cell* **128**, 1173–1186 (2007).
58. P. N. Kelly, M. J. White, M. W. Goschnick, K. A. Fairfax, D. M. Tarlinton, S. A. Kinkel, P. Bouillet, J. M. Adams, B. T. Kile, A. Strasser, E. Hall, Individual and overlapping roles of BH3-only proteins Bim and Bad in apoptosis of lymphocytes and platelets and in suppression of thymic lymphoma development. *Cell Death Differ.* **17**, 1655–1664 (2010).
59. A. R. D. Delbridge, S. Chappaz, M. E. Ritchie, B. T. Kile, A. Strasser, S. Grabow, Loss of PUMA (BBC3) does not prevent thrombocytopenia caused by the loss of BCL-XL (BCL2L1). *Br. J. Haematol.* **174**, 962–969 (2016).
60. J. D. Levenson, D. C. Phillips, M. J. Mitten, E. R. Boghaert, D. Diaz, S. K. Tahir, L. D. Belmont, P. Nimmer, Y. Xiao, X. M. Ma, K. N. Lowes, P. Kovar, J. Chen, S. Jin, M. Smith, J. Xue, H. Zhang, A. Oleksijew, T. J. Magoc, K. S. Vaidya, D. H. Albert, J. M. Tarrant, N. La, L. Wang, Z.-F. Tao, M. D. Wendt, D. Sampath, S. H. Rosenberg, C. Tse, D. C. S. Huang, W. J. Fairbrother, S. W. Elmore, A. J. Souers, Exploiting selective BCL-2 family inhibitors to dissect cell survival dependencies and define improved strategies for cancer therapy. *Sci. Transl. Med.* **7**, 279ra40 (2015).
61. V. Fresquet, M. Rieger, C. Carolis, M. J. Garcia-Barchino, J. A. Martinez-Climent, Acquired mutations in BCL2 family proteins conferring resistance to the BH3 mimetic ABT-199 in lymphoma. *Blood* **123**, 4111–4119 (2014).
62. P. Blombery, E. R. Thompson, T. Nguyen, R. W. Birkinshaw, J. Gong, X. Chen, M. McBean, R. Thijssen, T. Conway, M. A. Anderson, J. F. Seymour, D. A. Westerman, P. E. Czabotar, D. C. S. Huang, A. W. Roberts, Multiple BCL2 mutations cooccurring with Gly101Val emerge in chronic lymphocytic leukemia progression on venetoclax. *Blood* **135**, 773–777 (2020).
63. R. W. Birkinshaw, J.-n. Gong, C. S. Luo, D. Lio, C. A. White, M. A. Anderson, P. Blombery, G. Lessene, I. J. Majewski, R. Thijssen, A. W. Roberts, D. C. S. Huang, P. M. Colman, P. E. Czabotar, Structures of BCL-2 in complex with venetoclax reveal the molecular basis of resistance mutations. *Nat. Commun.* **10**, 2385 (2019).
64. M. L. Markwardt, G.-J. Kremers, C. A. Kraft, K. Ray, P. J. C. Cranfill, K. A. Wilson, R. N. Day, R. M. Wachter, M. W. Davidson, M. A. Rizzo, An improved cerulean fluorescent protein with enhanced brightness and reduced reversible photoswitching. *PLOS ONE* **6**, e17896 (2011).
65. R. N. Day, F. Schaufele, Imaging molecular interactions in living cells. *Mol. Endocrinol.* **19**, 1675–1686 (2005).
66. J. R. Lakowicz, *Principles of Fluorescence Spectroscopy* (Springer, 2006).
67. E. J. Osterlund, Q. Liu, D. W. Andrews, in *Mitochondrial Medicine* (Humana Press, 2015), pp. 395–419.
68. S. Koushik, H. Chen, C. Thaler, H. Puhl, S. Vogel, Cerulean, Venus, and VenusY67C FRET reference standards. *Biophys. J.* **91**, L99–L101 (2006).
69. A. Hopert, C. C. Uphoff, M. Wirth, H. Hauser, H. G. Drexler, Mycoplasma detection by PCR analysis. *In Vitro Cell. Dev. Biol. Anim.* **29**, 819–821 (1993).
70. K. Degenhardt, R. Sundararajan, T. Lindsten, C. Thompson, E. White, Bax and Bak independently promote cytochrome C release from mitochondria. *J. Biol. Chem.* **277**, 14127–14134 (2002).
71. F. Graham, J. Smiley, W. Russell, R. Nairn, Characteristics of a human cell line transformed by DNA from human adenovirus type 5. *J. Gen. Virol.* **36**, 59–72 (1977).
72. C. Lengauer, K. W. Kinzler, B. Vogelstein, Genetic instability in colorectal cancers. *Nature* **386**, 623–627 (1997).
73. K. A. Graham, J. M. Trent, C. K. Osborne, C. M. McGrath, M. D. Minden, R. N. Buick, The use of restriction fragment polymorphisms to identify the cell line MCF-7. *Breast Cancer Res. Treat.* **8**, 29–34 (1986).
74. L. Zhang, J. Yu, B. Park, K. Kinzler, B. Vogelstein, Role of BAX in the apoptotic response to anticancer agents. *Science* **290**, 989–992 (2000).
75. R. M. Kluck, E. Bossy-Wetzel, D. R. Green, D. D. Newmeyer, The release of cytochrome c from mitochondria: A primary site for Bcl-2 regulation of apoptosis. *Science* **275**, 1132–1136 (1997).
76. G. Hacker, The morphology of apoptosis. *Cell Tissue Res.* **301**, 5–17 (2000).
77. G. Brumatti, C. Sheridan, S. Martin, Expression and purification of recombinant annexin V for the detection of membrane alterations on apoptotic cells. *Methods* **44**, 235–240 (2008).
78. S. Kumar, D. Alibhai, A. Margineanu, R. Laine, G. Kennedy, J. McGinty, S. Warren, D. Kelly, Y. Alexandrov, I. Munro, C. Talbot, D. W. Stuckey, C. Kimberly, B. Viellerobe, F. Lacombe, E. W. F. Lam, H. Taylor, M. J. Dallman, G. Stamp, E. J. Murray, F. Stuhmeier, A. Sardini, M. Katan, D. S. Elson, M. A. A. Neil, C. Dunsby, P. M. W. French, FLIM FRET technology for drug discovery: Automated multiwell-plate high-content analysis, multiplexed readouts and application in situ. *ChemPhysChem* **12**, 609–626 (2011).
79. L. A. J. Alvarez, B. Widzowski, G. Ossato, B. Van Den Broek, K. Jalink, L. Kuschel, M. J. Roberti, F. Hecht, SP8 FALCON: A novel concept in fluorescence lifetime imaging enabling video-rate confocal FLIM. doi:10.1038/d42473-019-00261-x (2019).
80. U. Kaur, J. C. Lee, Unroofing site-specific  $\alpha$ -synuclein lipid interactions at the plasma membrane. *Proc. Natl. Acad. Sci. U.S.A.* **117**, 18977–18983 (2020).
81. N. Hirmiz, A. Tsikouras, E. J. Osterlund, M. Richards, D. W. Andrews, Q. Fang, Highly multiplexed confocal fluorescence lifetime microscope designed for screening applications. *IEEE J. Sel. Top. Quantum Electron.* **27**, 1–9 (2021).
82. C. Bruschini, H. Homulle, I. M. Antolovic, S. Burri, E. Charbon, Single-photon avalanche diode imagers in biophotonics: Review and outlook. *Off. J. CIOMP.* **8**, 2047–7538 (2019).
83. E. J. Osterlund, N. Hirmiz, C. Tardif, D. W. Andrews, in *Methods in Molecular Biology* (Humana Press Inc., 2019), vol. 1877, pp. 305–335.
84. T. Nagai, K. Ibata, E. S. Park, M. Kubota, K. Mikoshiba, A. Miyawaki, A variant of yellow fluorescent protein with fast and efficient maturation for cell-biological applications. *Nat. Biotechnol.* **20**, 87–90 (2002).
85. Z. Liang, J. Lou, L. Scipioni, E. Gratton, E. Hinde, Quantifying nuclear wide chromatin compaction by phasor analysis of histone Förster resonance energy transfer (FRET) in frequency domain fluorescence lifetime imaging microscopy (FLIM) data. *Data Brief* **30**, 105401 (2020).
86. R. N. Day, Measuring protein interactions using Förster resonance energy transfer and fluorescence lifetime imaging microscopy. *Methods* **66**, 200–207 (2014).
87. E. Butz, M. Ben-Johny, M. Shen, P. Yang, L. Sang, M. Biel, D. T. Yue, C. Wahl-Schott, Quantifying macromolecular interactions in living cells using FRET two-hybrid assays. *Nat. Protoc.* **11**, 2470–2498 (2016).

**Acknowledgments:** We thank D. Nguyen for helpful comments on this paper. **Funding:** This work was supported by Canadian Institutes of Health Research (CIHR) grant FDN143312 (D.W.A.), Canada Foundation for Innovation (D.W.A.), Ontario Ministry of Research and Innovation (D.W.A.), CQDM (D.W.A.), and Canada Research Chairs Program (D.W.A.). **Author contributions:** Conceptualization: E.J.O., N.H., and D.W.A. Methodology: E.J.O., N.H., and D.W.A. Software: N.H. Investigation: E.J.O., N.H., and J.M.P. Validation: J.M.P. and A.N. Visualization: E.J.O. Data curation: E.J.O. Supervision: D.W.A., B.L., and Q.F. Project administration: D.W.A. Writing—original draft: E.J.O. Writing—review/editing: E.J.O., N.H., J.M.P., Q.L., A.N., B.L., Q.F., and D.W.A. Resources: E.J.O., J.M.P., Q.L., and A.N. **Competing interests:** The authors declare that they have no competing interests. **Data and materials availability:** All data needed to evaluate the conclusions in the paper are present in the paper and/or the Supplementary Materials. There are no restrictions on the availability of materials. Table 2 includes source information of all reagents and links to the required software. All data needed to evaluate the conclusions in the paper have been uploaded to Scholars Portal Dataverse, with links in Table 2 for each figure that will be publicly available as of the date of publication. Uploaded data includes original Western blots, all screen platemaps, results of fitting analysis, and all binding curves corresponding to each square displayed in heatmaps of this paper. The binding curve data for each protein-protein interaction probed in the screen (Table 2, see link for each figure) may be further examined starting from analysis Step9\_FitCombinedData, by following our step-by-step analysis (Table 2, see Protocol Exchange). All original code for this paper was written by N.H. and has been deposited to Scholars Portal Dataverse (<https://doi.org/10.5683/SP3/QYDEDH>) with GPLv3 license (Table 2).

Submitted 12 October 2021

Accepted 1 March 2022

Published 20 April 2022

10.1126/sciadv.abm7375